INL/JOU-21-64332-Revision-1

Numerical analysis of dynamic load following response in a natural circulation molten salt power reactor system

August 2022

John P Carter, Richard Christensen, SuJong Yoon

Changing the World's Energy Future

Idaho National Laboratory

INL/JOU-21-64332-Revision-1

Numerical analysis of dynamic load following response in a natural circulation molten salt power reactor system

John P Carter, Richard Christensen, SuJong Yoon

August 2022

Idaho National Laboratory
Idaho Falls, Idaho 83415

http://www.inl.gov

Prepared for the
U.S. Department of Energy
Under DOE Idaho Operations Office
Contract DE-AC07-05ID14517

Numerical Analysis of Dynamic Load Following Response in a Natural Circulation Molten Salt Power Reactor System

JOHN P. CARTER*, RICHARD CHRISTENSEN, SUJONG YOON**

University of Idaho-Idaho Falls
Department of Nuclear Engineering and Industrial Management
1776 Science Center Drive, Idaho Falls, Idaho 83402

** Idaho National Laboratory
1955 N Fremont Ave
Idaho Falls, ID 83415

*john.carter@inl.gov

February 8, 2022

Number of pages - 34
Number of tables - 2
Number of figures - 13

Abstract

The Molten Salt Reactor (MSR) concept is a rapidly evolving Generation IV design that has recently attracted favorable attention due to the potential for reducing waste generation, realizing passive safety features, and seizing on the opportunity for cost effective economics. An investigation into the power transient behavior of an autonomous load following, natural circulation MSR system is important to quantifying operational and safety performance under dynamic conditions. This paper presents the results of a STAR-CCM+ and a comparative simple asymmetric, one-dimensional, finite-element numerical model to solve the compound dynamic MSR power behavior subject to flow and temperature reactivity feedback only. Results show that reactor power is affected by fuel salt flow velocity (global) and temperatures (local) in a coupled, time-delayed manner that results in a unique compound dynamic closed-loop power feedback mechanism. This novel simulation approach opens the possibility of performing inexpensive computations to evaluate time-dependent reactor performance relative to thermo-physical fuel salt limitations. Natural circulation MSRs are stable and potentially provide a leap in safety and reliability.

1 Introduction

Molten salt reactors (MSRs) were first developed over a half a century ago. With the advent of new materials, fabrication methods, and analysis tools there has been increasing interest in this type of reactor around the globe. MSR concepts have gained renewed interest in Japan, Russia, China, France, and the USA. One of the six Generation IV designs selected for further development by the Generation IV International Forum (GIF) is the MSR. The GIF was initiated by the US Department of Energy in 2000 and formally chartered in mid-2001. Several early innovators have entered the design and licensing arena, including Flibe Energy, ThorCon, Moltex, Seaborg Technologies, and Terrestrial Energy. An integral molten salt fast reactor (MSFR) Euratom project named EVOL is also being considered by a European Consortium consisting of six European countries including France, Germany, Hungary, Italy, the Netherlands, and the United Kingdom. MSRs are considered among the Generation IV reactor concepts due to their potential to realize non-proliferation, manageable waste stream, and sustainable global energy needs around the globe (IAEA, 2013). New ideas are being pursued that were once thought to be too expensive or intractable. For instance, the improving availability of high-end computing resources and development of robust numerical multi-physics computational methods and applications have made design, evaluation, and demonstration of advanced nuclear concepts and engineering designs more achievable than ever before. Concepts and designs can be modeled, analyzed, and evaluated long before resources are allocated for more cost-effective prototypic demonstrations.

A small, thermal spectrum, natural circulation MSR design (novel Molten Salt Nuclear Battery - MsNB concept) notionally uses a molten salt fuel at low pressure and high temperature and consists of a self-contained primary system within a single structural vessel. The heat source, heat sink, and heat exchangers are contained within a single integral reactor vessel. The MsNB achieves autonomous load following such that reactor core power follows heat exchanger power demand through a compound dynamic temperature and low feedback mechanism without operator intervention. The potential exists for future MSR designs to optimize core physics, fuel salts, and innovative fuel cycle management schemes that have significant opportunities to reduce fuel loading to fractions of current Light Water Reactors (LWR) which may also reduce production of Pu and Transuranic (TRU) waste products.

The MsNB design concept presented in this investigation provides continuous 400kW thermal power for a duration of 10 years. The reactor is fueled by HALEU (19.75% enrichment U-235) uranium tetrafluoride mixed at 18 mol% in a FLiNaK salt euctectic. The reactor stands 2.2 meters in height and 1.5 meters in diameter. This investigation shows the reactor has self-limiting, stable power behavior that maintains safety margins to fuel salt solubility, freezing, and vaporization limits. Nominal reactor operating parameters are 600-700 degrees Celsius, 170 kpa pressure, and sustains a mass flow rate of 35-45 kg/sec with a differential temperature across the core of 32 degrees Celsius at full rated power. The power can be upscaled to over 1 MWe without incurring fuel loading penalties such as enrichment or fuel salt solubility limits. Full scale, the MsNB can operate up to 5-10 MWe. End-to-end fuel cycle evaluations presented in this investigation demonstrate that the MsNB concept is feasible while providing environmentally safe and reliable power generation for a decade. Physical and neutronics MsNB parameters are provided in Table 1 and Fig.1. MsNB linear dimensions are provided in Table 2.

Understanding the time-dependent behavior of this liquid fueled natural circulation reactor system is of particular interest since reactivity changes due to core flow rate causes an inherently destabilizing effect on reactor power. Decreasing system flow, for instance, has a positive reactivity effect on the core because proportionally fewer delayed neutron precursors advect out the core and produce added delayed neutrons in the core. This might occur when heat exchanger power demand decreases. In a situation where power demand decreases, the heat exchanger outlet and average cold leg temperature initially raises which causes a reduction in downcomer fuel salt density. This reduction in density causes an accompanying reduction in hot and cold leg differential pressure and system flow rate. Therefore, as heat exchanger power demand on the reactor system decreases the reactor power generation increases due to fuel salt flow changes. The reverse effect occurs for increases in system power demand. This mechanism is referred to as *flow reactivity*. A time-delayed temperature mechanism associated with the arrival of the colder fuel at the core inlet inserts negative reactivity and eventually corrects the opposing power demand behavior. This temperature reactivity effect is common in traditional solid fuel designs, the flow reactivity mechanism is unique to liquid fueled reactors and as a volumetric effect is less well understood. These two counter-acting compound dynamic feedback reactivity effects are modeled using Python code to investigate the stability of such a thermal-neutronic system.

The implementation of passive cooling and heat transfer in thermal engineering has resulted in high reliability and compact size in system design. Many studies have been conducted to understand the stability and characterization of flow dynamics in natural circulation systems in single phase and two-phase flow regimes. In the mid-1960s, Welander and others published seminal works studying the flow stability of differentially heated loops (Welander, 1967). Many extended this work and further characterized flow dynamics and the nature of instabilities of natural circulation fluid systems in the application of passive energy removal in nuclear applications. The phenomenology of flow instabilities is manifestly chaotic due to the non-linear nature of the energy and momentum conservation equations that govern the fluid behavior. For this reason, numerical analysis is often well suited to provide insight into dynamic system behaviors. Pini, for instance, showed that stability improves with internal heated fluids (Pini, 2016). Using numerical analysis, Desrayand and others showed the significant effect of the Reynolds number on the flow characteristics in the loop (Desrayandi et al, 2005)(Desrayandi, 2013). Nayak also used numerical techniques to investigate stability characteristics of a natural circulation loop and the effects of nanofluids on flow behaviors which is germane to the ”ionic soap” that is the salt fuel, i.e. fission product nanofluid (Nayak, 1995)(Nayak et al, 2005).

This investigation uses a one-dimensional simplified model to evaluate the effects of two opposing, time-delayed reactivity mechanisms that act as the principle feedback to enable autonomous, power-following reactor control. The compound dynamic feedback is unique to liquid fueled reactors and natural circulation during power operations makes flow reactivity a significant power control feature. Basic reactor power response to heat demand transients is central to this investigation. Thermal transient behavior will provide an evaluation of proximity to thermophysical fluid limitations.

Fuel Salt flow is convective driven by density differences between the reactor hot and cold thermal centers. Consequently, reactor flow will be dependent on fuel salt density variations due to heat

exchanger demand and system energy balance during operations. A down-power demand on the heat exchanger, for instance, will initially drive heat exchanger outlet temperature higher and gradually reduce the overall cold leg density. This gradually reduces the overall system differential pressure and consequently also reduces system and core flow until colder fuel temperatures arriving at the core result in a positive reactivity addition due the negative temperature coefficient of the core (-3.5 pcm/K). The initial reduction in core flow causes a positive reactivity effect due to fewer delayed neutron precursors exiting the core and producing fractionally more delayed neutrons inside the core (Pazsit, 2017). These neutrons would otherwise be produced outside the core and not contribute to the critical neutron economy. This flow reactivity effect is unique to MSR dynamic performance and must be considered in time-dependent power response of the system and safety basis analysis. Therefore, a down-power in system energy demand causes an initial reactor power increase. Conversely, if the heat exchanger undergoes a up-power demand, then the initial reactor power response is downward. This unstable, contravariant nature of power response in a natural circulation MSR is of great interest and must be shown to be controllable or limited under all credible operating conditions. Moreover, slow natural circulation transport times prolong reactor power response time and amplifies the power and temperature over and under shoot behaviors under dynamic powering conditions. The same is true for heat exchange down-power demands, that initially cause upward reactor power excursions due to increased system flow. Concerns for the potential for fuel salt solubility, fuel freezing, or fuel salt vaporization must be considered in the safety case basis. This behavior will be further analyzed and modeling in this project.

Once fuel salt flows through the core and is fission heated, the fuel flow vertically through the chimney where a fraction of neutrons that either leak from the core or are generated by the decay of delayed neutron precursors are reflected downward by beryllium reflectors that do not impede the convective flow. At the top of the chimney the flow diverges into a horizontal plane and enters the primary heat exchanger inlet. Once in the heat exchanger, the flow continues radially outward and then downward where the flow stream is cooled, and fuel salt density increases to provide the net thermal driving head to continue the closed loop flow cycle.

An investigation of the power transient behavior of the MsNB was undertaken in this study. Power reactor traditionally have a power following behavior between the heat exchanger and the core. As power demand on the system changes, reactor power follows to meet heat exchanger demand. In a traditional solid fueled reactor system with negative temperature coefficients this following behavior is automatic and inherent to core physics behavior. The MSR is fundamentally different in power response. In addition to a less dominant temperature coefficient, the MSR is also affected by flow reactivity effects. In a natural or convective flow MSR system such as the MsNB flow reactivity effects can dominate the reactor's response to power transients. For instance, take a down power demand on the heat exchanger. A down power on the heat exchanger results in an increase in heat exchanger outlet temperature that propagates down the downcomer and eventually enters the core. In the MsNB this flow transfer takes about 30-60 seconds. Since the downcomer temperatures decrease, the corresponding downcomer densities increase. This increases the differential pressure between the hot core leg and the colder downcomer region. The increases differential pressure results in increase flow in the system. The resulting increase in system flow produces a negative reactivity in the core and a decrease in reactor power. So, the reac-

tor power follow behavior manifest in traditional reactor system is not true in MSR convective system. This downward power trend will continue until the colder fuel salt enters the core in sufficient rate and volume to turn reactor power upward due to the negative temperature coefficient. Once the temperature coefficient turns reactor power the downward power excursion may be significant due to the slow loop transport times. Eventually reactor power will recover and overshoot to help restore the system heat balance. This overshoot results in continuing flow and power oscillations that may or may not be stable. Loop transport time, flow and temperature coefficients play a significant role in system stability.

Flow reactivity can be viewed as an effect caused by global (loop-wide) thermal properties which affects the flow velocity. Temperature reactivity on the other hand is a local effect based only on the temperatures in the core. The interplay of these two core physics effects determine reactor power response to thermal-hydraulic dynamics in the MSR system.

2 Fuel Salt Flow Phenomenology

2.1 Thermal Hydraulics in a Natural Convection MSR System

Buoyant convective flow in a closed loop system is driven by fluid average density differences between hot and cold legs of the system. Density differences are established when the cold thermal center (region of lowest average system temperature) is placed above the hot thermal center (region of highest average system temperature). In the MSnB design the reactor core is placed low in the loop system just above the core inlet plenum region and the primary heat exchanger is placed high in the loop at the reactor top outlet plenum region, see Fig.1. Due to the offset placement of the heat exchanger the hot and cold legs are asymmetric in their flow cord lengths. The effective vertical height difference between core center and heat exchanger center in the MsNB design is about 1.09 meters. An average density difference between hot and cold leg fuel salt is about 10-20 kg/m^3 which establishes a differential pressure in the system of about 200-250 Pascal. This results in a flow rate of about 5.0 cm/s in the system assuming the pressure loss coefficient, ξ, is about 25. This assumption is validated by STAR-CCM+ modeling results that include frictional energy losses.

Generally the hydraulic relationships that apply in the convective flow case are,

$$P_{\mathrm{out}} = P_{\mathrm{in}} + \rho\left(\frac{v_{\mathrm{in}}^2 - v_{\mathrm{out}}^2}{2}\right) + \rho g\left(z_{\mathrm{in}} - z_{\mathrm{out}}\right) - \xi\frac{\rho\bar{v}^2}{2} \tag{1}$$

and

$$h_{\mathrm{out}} = h_{\mathrm{in}} + \left(\frac{v_{\mathrm{in}}^2 - v_{\mathrm{out}}^2}{2}\right) + g\left(z_{\mathrm{in}} - z_{\mathrm{out}}\right). \tag{2}$$

For this model, fluid height or velocity are assumed to have negligible change in fluid enthalpy.

The differential pressure of the closed-loop, bouyant convective flow system can be written in terms

of the average hot and cold leg density,

$$\Delta P(t) \quad = \quad (\bar{\rho}_{\mathrm{cold}}(t) - \bar{\rho}_{\mathrm{hot}}(t))\, hg \tag{3}$$

where ΔP is the system differential pressure, ρ is the average hot or cold leg density, h is the difference in system thermal centers, and g is the gravitational constant. This differential pressure establishes flow in the loop at a magnitude sufficient to overcome the resistive drag force in the system. Friction losses can result from forces on flow surfaces and the flow system geometry that result in changes in flow direction or can present hydraulic resistance to flow inertia, i.e. heat exchanger, core internals, elbows, and flow direction devices (IAEA, 2005)(Manohar, 2013). System resistance can be written as,

$$\Delta P(t) \quad = \quad \left(f \frac{L}{D_H} + \sum K \right) \frac{\bar{\rho} v^2(t)}{2} \tag{4}$$

$$= \quad \xi \, \frac{\bar{\rho} v^2(t)}{2}. \tag{5}$$

The first term is the straight pipe resistance where f is the Darcy friction factor, L is the pipe length, and D_H is the hydraulic diameter of the flow volume. The second term are local form losses, K, due to flow restrictions such as elbows, circuitous heat exchanger flow path, and changes in inlet and outlet plenum flow direction. The two terms combined are the system pressure loss coefficient (PLC), ξ. An estimate of the PLC was used in this investigation based on standard pipe fitting coefficients (Janna, 1998) and previous analysis of the heat exchanger PLC of 7.0 (Cardenas-Melgar, 2021).

The system velocity can then be determined by,

$$v(t) \quad = \quad \sqrt{\frac{2\ \Delta P(t)}{\xi\, \bar{\rho}}} \tag{6}$$

where $\bar{\rho}$ is the system average fuel salt density. System flow varies as the inverse square root of the system pressure loss coefficient. Therefore, as pressure losses increase system flow decreases in an inverse square root proportion. Since this parameter affects system flow, it also may affect power over and under shoots during power demand transients. This will be examined in the results section.

A constant heat exchanger wall temperature and uniform volumetric internal heating rate is assumed. As a result, temperature variations and heat transfer within the reactor core and the primary heat exchanger are assumed to change linearly over fluid travel distance in the heat source or sink. Reactor core and heat exchanger differential temperatures are approximated using heat transfer equations,

$$\dot{Q}(t) \quad = \quad \dot{m}(t)\, c_p(\bar{T}(t))\ [T_{\mathrm{out}}(t) - T_{\mathrm{in}}(t)]\,. \tag{7}$$

Eq.7 is used in the model to determine the core and heat exchange outlet temperature after time-step

values for reactor power, heat exchanger power, system mass flow rate, and specific heat capacity are calculated. $\bar{T}$ is the heat source or sink average temperature. All the quantities in Eq.7 are functions of time.

Fuel salt density is a function of composition and temperature. Salt density can be determined using the weight percent relationship,

$$\frac{1}{\bar{\rho}} = \sum_i \frac{w_i}{\rho_i} \tag{8}$$

where $\bar{\rho}$ is the mixed fuel salt density, w_i is the weight percent of constituent i, and ρ_i is the density relationship of constituent i. Using this relationship for 15 mol% UF_4 in a FLiNaK eutectic composition mix (46.5-11.5-42 mol%) gives a temperature dependent density relationship of,

$$\rho_{\text{density}}\ [\text{g/cm}^3] = -9.4601046\,\text{x}\,10^{-4}\ \text{T[K]} + 4.6820365 \tag{9}$$

where density is in g/cm^3 and fuel salt temperature, T, is in Kelvin. The specific heat capacity of FLiNaK fuel salt is,

$$c_p\ [\text{J/kg} \cdot \text{K}] = 1.0634\ \text{T[K]} + 976.78 \tag{10}$$

where c_p is in J/kg-K. Mass flow rates are easily calculated using the $\dot{m} = \rho A v$, where A is the MsNB cross sectional flow area ($\approx 0.4\text{m}^2$) (Manohar,2013)(Guifeng, 2019)(Lizin, 2013).

2.2 Density Wave Oscillations

The direction and stability of flow is determined by the temperature difference between varying locations in the loop where buoyant forces are relevant. These propagating temperature variations result in fluid density variations that can induce flow and power oscillations. Temperature oscillations driven by changes in core reactivity result in fluid density and pressure changes in the system. For this reason, flow velocity can oscillate or reverse direction depending on external factors that influence system energy. The goal of most past studies was to evaluate for the predictive operating conditions where instabilities can be expected. Avoiding or implementing mitigating controls near unstable or chaotic flow regimes is desirable from a design safety standpoint.

While significant work has been completed to examine the mechanisms of single phase and two-phase flow in light water reactor system, virtually no work has been conducted to investigate the flow stability of a closed-loop, natural circulation molten salt reactor system. The engineering study of such a system is currently under investigation with the MsNB at the University of Idaho.

Thermal hydraulic instabilities that result from closed-loop, natural circulation flow are generally classified into two categories: static and dynamic. The MSR has a unique instability mechanism caused

by reactivity effects coupled to delayed neutron precursor advection. Namely, molten salt velocity in an MSR system influences the fraction of transported precursors from the core and therefore affect core reactivity. As a result, reactor power and local system temperatures respond to flow velocity changes. The contribution of precursor advection to the system's thermal hydraulic feedback is unique and not well studied experimentally. Furthermore, traditional density wave oscillations are caused by time delayed feedback effects between flow, temperature, and pressure fields in the closed loop. Temperature oscillations in the closed loop cause in-phase time variation of fluid density. Density wave oscillations are well understood in closed-loop, natural circulation systems. Density wave oscillations coupled with power changes induced by flow reactivity effects result in compound dynamic interactions that have both temporal and spatial delayed feedback contributions to reactor power and have been studied less. Combined, both interact in a time-dependent manner to generate a combined dynamic instability unique to molten salt fueled systems.

2.3 Compound Dynamic Effects Unique to MSR - Flow Reactivity Coefficient

Compound dynamic effects (CDE) generate a unique class of time-dependent power behaviors that occur when in addition to fundamental effects such as density variations, secondary effects are involved that couple to and significantly modify the fundamental system response. A typical case of a fundamental effect is density wave oscillations caused by the delay and feedback between fluid flow, density, and pressure in a closed-loop system. The MSR has a characteristic CDE that is unique to flowing fuel systems that results from two reactivity affecting changes, namely, average core temperature (fundamental) and delayed neutron precursor advection (secondary). Precursor advection results in delayed neutrons being generated in locations other than where the precursor is produced. This non-local contribution to the neutron economy introduces flow dependent reactivity effects, i.e. *flow reactivity*. This specific CDE as it relates to the MSR will be referred to as the *compound reactivity effect*. Compound reactivity effects are similar to the interaction between void reactivity and flow dynamics and heat transfer in a boiling water reactor (BWR). In a MSR, flow reactivity couples to the thermal-hydraulics of the system.

The compound reactivity effect has two opposing reactivity mechanisms. The first mechanism is related to the temperature coefficient of reactivity that also acts in traditional solid fueled reactor systems. As core average temperature changes, the core reactivity changes due to Doppler absorption and material density changes. For the MsNB, the temperature coefficient was determined to be about -3.5 pcm/K across the 600-700 degrees Celsius operating temperature range of the reactor (Carter, 2021). The temperature reactivity in the core can be calculated by,

$$\Delta\rho_T(T) \quad = \quad \alpha_T(T)\,\Delta T \tag{11}$$

where α_T is the temperature coefficient of reactivity and ΔT is the change in average core temperature. The temperature coefficient is assume constant over the range being considered (800-1000 K).

The second reactivity mechanism is unique to flowing fuel systems. As fission products advect out

of the core, delayed neutron precursors are transported from point of generation to the point of decay. The point of decay may be out of the active core region (ex-core) which results in a loss of neutron inventory to sustain criticality. Using a one-group delayed neutron precursor (DNP) model, on average the number of DNPs that decay outside of the core is a function of time spent out of the core versus time spent in the core. The relative times the DNPs spend in the transport cycle are determined by loop geometry and fuel salt transport velocity. In the one dimensional case, near critical conditions, the core neutron multiplication factor can be expressed as,

$$K_{eff} \simeq 1 - f(u)\beta_{eff}, \tag{12}$$

and hence,

$$\rho_f(u) = -\frac{f(u)\beta_{eff}}{1 - f(u)\beta_{eff}}, \tag{13}$$

where $f(u)$ is a velocity dependent function for the fraction of precursors outside of the core and β_{eff} is the static delayed neutron fraction. The function $f(u)$ can be thought of as one minus the ratio of the β_{eff} for the circulating system to the β_{eff} for the static case as shown in eq.18. The departure from criticality is proportional to the fraction of precursors that advect out of the active core region. So a static fuel condition, all precursors remain in the core and the reactor remains critical. As fuel salt velocity increases, more precursors decay outside of the core and do not contribute neutrons to criticality. As flow velocity increases to large values such that loop recirculation time is much shorter than precursor group decay half-life, an asymtotic neutron loss is reached as precursors that leave the reactor return before decay occurs. In the limit of large flow velocities, the fraction of delayed neutrons produced outside of the core is the time spent in the loop outside the core over the total loop recirculation time. For simplicity it is assumed that flow velocity is the same throughout the system loop at any location and moment in time (ρA = constant; where A is the cross sectional flow area), therefore the fraction of delayed neutrons produced outside of the core is directly related to the loop and core flow cord lengths. Specifically, in the limiting case for large fuel salt velocities, K_{eff} is given by,

$$K_{eff} \simeq 1 - \left(\frac{L}{L+H}\right)\beta_{eff}, \tag{14}$$

where L is the ex-core loop length and H is the in-core flow cord length. As the ex-core loop length becomes very large such that recirculation time is large compared to precursor half-lives then the multiplication factor approaches 1-β_{eff}. The expression for the large velocity limit for core reactivity is then given by,

$$\rho_\infty = -\frac{\beta_{eff}}{(1-\beta_{eff}) + \frac{H}{L}}, \tag{15}$$

where for large L the reactivity penalty at high flow rates is a function of the delayed neutron fraction

only. Dulla's previously published work shows that the functional form for reactivity changes in a MSR core due to velocity changes (inital stationary fuel flow) can be expressed as,

$$\Delta\rho_f(u)\mid_{0\to u} \;\simeq\; \rho_\infty\left(1 - e^{-\alpha_f u}\right), \tag{16}$$

where α_f is referred to as the flow reactivity exponent and is determined by linear regression of Dulla numerical results (Dulla, 2005) and is provided in Table 1. It is assumed that the value of α_f is the same between the Dulla's results and the MsNB. The two system have similar β and system loop length ratios and at velocities above 4 cm/sec the reactivity changes are insensitive to velocity effects. The flow reactivity exponent is a function of core physics. The change in flow reactivity between an initial velocity, u_i and final velocity, u_f can be written,

$$\Delta\rho_f\mid_{u_i\to u_f} \;\simeq\; \rho_\infty\left(e^{-\alpha_f u_i} - e^{-\alpha_f u_f}\right). \tag{17}$$

Analytically, the fraction of precursors that advect outside the active core volume can be expressed as a normalized ratio of precursor concentrations integrated over the core volume as a function of fuel salt velocity. Specifically,

$$f(u) \;=\; 1 - \left(\frac{\int C_o(u,\vec{\mathbf{r}})\,dV}{N}\right), \tag{18}$$

where C_o is the static (time-independent) precursor concentration distribution function (normalized to core integrated flux). The second term is the circulation β_{eff} to static β_{eff} ratio. For a 1-D model, this relationship reduces to a definite integral over the axial dimension, $-a$ to a. N represents the precursor number at zero flow or,

$$N \;=\; \int C_o(0,\vec{\mathbf{r}})\,dV. \tag{19}$$

The static flux and precursor equations can be numerically solved to provide C_o. Although it can be shown that the approach used in Eq.18 and 19 provides a statistical coefficient of determination $>$ 0.99 R^2 fit to analytical, deterministic, and Monte Carlo agreements in previous published work by M. Aufiero, this paper will use a regression fit of Dulla's results (fit with $>$ 0.98 R^2) and shown by Eq.16 (Aufiero, 2014; Dulla, 2005). This provides simplification without significant lose in technical rigor in the results. For the parameters provided in Table 1 and used in this analysis, ρ_∞ = 499 pcm. Notice that as velocity becomes large, the change in flow reactivity becomes small for incremental changes in velocity. This is because at larger velocities (velocities that allow the fuel salt to traverse the loop within the one-group decay constant) the precursors are effectively distributed through the loop and the rate of precursor loss from the core is offset by the precursors returning to the core and no net additional neutron loss is noted. Both reactivity mechanisms affect core power response in a coupled, non-linear manner. Fig.2 diagrammatically illustrates this compound reactivity effect.

As can be seen, the flow reactivity coefficient is strongly dependent system geometry and fuel salt flow velocity. This opens a rich area for engineering inputs that can affect core performance outcomes.

3 Modeling Approach

The sum of flow and temperature reactivity affects core power. Each finite element time-step performs a calculation to determine the reactor period, τ. This can be written as,

$$P[t+1] \quad = \quad P[t]\, e^{[t]/\tau} \tag{20}$$

the square brackets denote numerical time-step iterations. One-group kinematics provides a formulation for calculating the flow dependent reactor period, namely

$$\tau(u,t) \quad = \quad \frac{l^*}{\rho(t)} + \frac{(1-f(u))\beta_{eff} - \rho(t)}{\lambda\rho(t) + \dot{\rho}(t)}, \tag{21}$$

where l^* is the prompt neutron generation time, ρ is the total core reactivity (flow and temperature reactivity summed), λ is the delayed neutron precursor one-group decay constant, $(1-f(u))$ is the fraction of precursors in the core (1.0 when u=0 cm/s) and $\dot{\rho}$ is the time rate of change of reactivity (Lamarsh, 2001; Duderstadt, 1976). Precursors advecting out of the core have the effect of reducing the circulating β_{eff} and diminishes the contribution the second term has on reactor period. The time dependence of each factor is made explicit in the equation to emphasize implications on the time-step numerical solution method. The first term provides the prompt neutron contribution to the time rate of change of reactor power while the second term provides the delayed neutron contribution. The time rate of change of reactivity in the second term plays a significant role in the compound dynamic effects in the MSR.

Python 3.7 was used on a linux, 12-core, Lenovo ideapad 330S to develop a time dependent finite-element code to model the thermal hydraulic and neutronic coupled flowing loop. This section outlines the approach taken to solve the time iterated system frames. Fig.3 outlines the model coding methodology. Constants in this model included the temperature and flow coefficients of reactivity, the prompt neutron generation time, the effective delayed neutron fraction, the one-group delayed neutron decay constant, the system pressure loss coefficient (PLC), constants associated with fuel salt density computations, thermal center heights, and core dimensions. Global (time-dependent) and local (time and space-dependent) array variables and functions were used in this application. Global variables and functions are reactor power, heat exchanger power demand, differential pressure between hot and cold legs, system fuel salt velocity, flow and temperature reactivity in the system, reactor period, average specific heat capacity of the hot and cold legs, average reactor and heat exchanger temperature, time rate of change of reactivity, and differential temperature across the reactor and heat exchanger. Local variables included temperature and density. The time rate of change of reactivity in the system was determined by standard finite difference approximation.

Differential temperatures across the reactor and heat exchanger and outlet temperatures were calculated at each time step using Eq.7 based on time-step values of inlet temperature, system mass flow rate, and hot/cold leg specific heat capacity.

3.1 Finite Element Spatial Propagators

At each time-step, global variables are calculated based on the results of a nested spatial computation loop that updates local variables. Specifically, local variables such as temperature and density are space-advanced (incremented) based on system mass flow rate, $u(t)dt$. As shown in Fig.4, advancing by $u(t)dt$ each time step mimics the convective transport of the fuel salt in the system loop. For example, reactor outlet temperature cell is advanced toward the heat exchanger inlet by a distance the volume would travel in a time-step interval.

After the spatial local variables are spatially advanced, the code calculates updated average reactor and heat exchanger inlet temperature values. Inlet temperatures are calculated using an averaging routine that accounts for heat exchanger fluid mixing at the inlet. The code then calculates updated average vertical hot and cold leg densities. The densities are assumed to change linearly in the reactor and heat exchanger. Spatially advancing reactor and heat exchanger exit temperatures and densities ensures fluid propagation at rate commensurate with fluid velocity to the down stream heat device.

The code then updates all global variables for time step [t] and then calculates updated reactor and heat exchanger outlet temperatures using time history heat balance,

$$T_{\mathrm{Rx,Outlet}}[t] \quad = \quad T_{\mathrm{Rx,Inlet}}[t-1] + \Delta T_{\mathrm{Rx}}[t-1] \tag{22}$$

and,

$$T_{\mathrm{Hx,Outlet}}[t] \quad = \quad T_{\mathrm{Hx,Inlet}}[t-1] - \Delta T_{\mathrm{Hx}}[t-1]. \tag{23}$$

Once all global and local array variables are computed the time-step is incremented and the computation is repeated until the model simulation is complete. Generally, at 400 kW thermal output the steady-state system parameters are loop differential pressure is 230 Pa, flow velocity is 5 cm/s, and reactor differential temperature is 32 degrees Celsius.

3.2 Boundary Conditions

Time delayed boundary conditions are appropriately applied to ensure energy conservation and flow is recursive in the closed loop. Two temporal boundary conditions are important is this model. First, fluid arriving at the reactor inlet originated at an earlier time dependent on flow rate leaving the heat exchanger outlet. Similarly, fluid arriving at the heat exchanger inlet originates at an earlier time leaving

the reactor outlet region. For the purposes of simplification, flow velocity is assumed to be constant throughout the closed-loop circulation path. Changes in flow velocity due to changes in flow area, for instance, can be scaled into the model if needed. One spatial boundary condition is imposed to ensure that loop is closed. Mathematically these boundary conditions are written in the local temperature arrays as,

$$T[RxInlet, t] \quad = \quad T[HxOutlet, t - \frac{l_d}{u}], \tag{24}$$

$$T[HxInlet, t] \quad = \quad T[RxOutlet, t - \frac{l_c}{u}], \tag{25}$$

and

$$T[RxInlet0,\ t] \quad = \quad T[RxOutlet1,\ t]. \tag{26}$$

where l_d and l_c are the downcomer and chimney flow length, respectively.

3.3 Assumptions

Assumptions are introduced to aid in model simplification without significant lose of physical rigor. First, the model is one-dimensional and assumes adiabatic conditions in piping between the heat exchangers. Fission heating is assumed to be uniform in the core and results in a linear temperature rise in the fuel salt through the core. Actual fuel salt temperature is a function of axial height in the core due to varying distributions of thermal flux and fission cross sections. The core outlet temperature calculation is assumed to be a simple function of inlet temperature, average core fuel salt heat capacity, mass flow rate, and reactor power. In addition, average core temperature is weighted to 60% toward outlet to accommodate axial flux skewing to upper core due to precursor convention. The core is assumed to have a constant temperature coefficient across the range of investigated temperatures (values provided in Table 1). The Doppler coefficient was found to be relatively insensitive to temperature in the nominal operating range of $600 - 700^{o}$C (Carter, 2020b). The core and heat exchanger inlet temperatures are assumed to be a 20 centimeter spatial average of the fluid temperature. This accounts for an expected amount of inlet mixing that would be present in the system.

Changes in spatial and temporal values over successive finite elements are small compared to rates of convective and reactor period changes and for this reason errors inserted due to finite element methodology are assumed small. The 571 cm loop is divided into equally spaced one millimeter spatial elements while temporal computations are divided into one second intervals. The selected element sizes are reasonable based on average thermal and temporal gradients calculated in the model. Additionally, axial fluid heat conduction is assumed negligible and fluid properties with exception of density and heat capacity are assumed to be constant. Fluid axial heat conduction must be considered if the Peclet number

is on the order of one or less. The Peclet number, Pe, for the hot and cold legs is provided by,

$$Pe = \frac{\rho_o c_p u L}{k}, \tag{27}$$

where ρ_o is the reference fluid density, c_p is the specific heat capacity, u is the fluid speed, L is the fluid segment characteristic length, and k is the thermal conductivity. The Peclet number is a dimensionless representation of convection-to-conduction energy transport in the fluid. For the MsNB using FLiNaK the Peclet number is in excess of 25,000 and therefore heat transfer by conduction is negligible. It should be noted than at low power heating conditions conduction may have a much larger contribution to system heat transport and may need to be considered. Low power flow modes are beyond the scope of this investigation and left for future work. Finally, this model assumes constant pipe size, uniform heat flux in the heat and cooling section, and combines friction pressure losses due to varying pipe sizes into a single pressure loss coefficient K as defined in Eq.4.

The form of the flow reactivity provided in Eq.15 is obtain by regression of numerical results calculated by Dulla (Dulla, 2005). It is assumed that this form holds in the physical case. The value of flow reactivity exponent, α_f used in this paper (Table 1) is an approximation to the actual value and it is assumed that difference will not insert significant changes in the modeled results. Flow exponent sensitivity analysis indicates the results to the first order are insensitive to changes in the flow coefficient.

3.4 STAR-CCM+ modeling of transient behavior - a validation of the 1-D approach

A STAR-CCM+ java macro script developed in collaboration with SuJong Yoon of the Idaho National Laboratory using the core physics modeled in the python code (Siemens, 2020). The objectives of the CFD modeling and the necessary of three-dimensional CFD modeling is to provide a first-principle-based approach to determining the pressure loss coefficient in Eq 5. A macro was developed to calculate a time step value for flow and temperature reactivity using STAR-CCM+ field function calculated values for average volumetric core temperature and average core outlet surface averaged axial fluid velocity in the buoyant, closed-loop convective system. The physics solver configuration adopted for this model includes use of the K-Omega all wall Y+ treatment, gravity gradient, Reynolds-Averaged Navier-Stokes turbulance, second-order segregated flow, nearest neighbor solution interpolation, and shear-stress transport K-Omega three-dimensional turbulent flow model. STAR-CCM+ and the author developed Python code used the same physics model outlined by Eq. 21. STAR CFD results were then used to inform the 1D Python code thermal-hydraulics to more closely generate the high fidelity CFD results. CFD informed modifications primarily involved adjustments to the 1D fluid temperature spatial averaging at heat exchanger transitions which affected the magnitude and duration of thermal-hydraulic and power responses to transients. This numerical approach produced a 1D Python code that produces meaningful simulated results without the expense computational overhead associated with STAR-CCM+. A typical 2400 second physical time STAR simulation using 48 HPC cores nominally results in a total solver elapse time of approximately 63 hours to complete a transient simulation. The CFD informed 1D Pytho code can run the same transient in roughly 10 minutes utilizing single core processing on a Lenevo ideapad 330S laptop while providing improved confidence in results. For this reason, this investigation will

present Python code results based on CFD informed simulation results using a java macro to calculate core physics.

Two specific modifications were made to the author developed Python code that simulates the MSR power following, natural circulation power transient code. First the system pressure loss coefficient (PLC), ξ, was adjusted to replicate system flow velocities provided by STAR-CCM+ using smooth wall surface conditions. The PLC was calculated by STAR-CCM+ to be approximately 11.0 for the configuration operating at 400 kW. Secondly, the Python code was modified slightly to accommodate some degree of fluid mixing at the heat inlets. This aided in smoothing the thermal-hydraulic results that more closely represented the STAR-CCM+ thermal hydraulic calculations in pressure, flow, and temperature.

While modeling and simulation verification, validation and accreditation of the author's Python code is difficult if not possible at this time due to the absence of real-world experimental data to compare simulation results, the author's intent in this dissertation is to show the Python code provides reasonable simulation results commensurate with the accredited CFD code such as STAR-CCM+ under limited evaluated situations. An investigation into mesh sensitivity on simulated STAR-CCM+ results indicated a uniform mesh base size of 8 mm resulted in reasonable independence in simulated results. Specifically, varying mesh base size from 6 mm to 12.5 mm changed calculated mass flow rate by 1.9% and core dofferential temperature by 3.7%. Using this approach, the author considers the STAR-CCM+ simulation results a high fidelity thermal-hydraulic simulation that provides confidence in CFD computed results with the physics provided. Under these limited conditions, the author considers his Python code a viable option that provides reasonable results at significantly less computational expense.

Fig. 5 illustrates the results of a STAR-CCM+ time-dependent transient power simulation for a MSR configuration. Initial system power is 400 kW stead state. At time zero the system experiences a prompt power demand increase to 4 MW for a duration of 130 seconds which corresponds to the time needs to flow reactivity dominance to subside. At time 130 seconds, the system power demand decreases to 0 kW. The initial reactor power response decreases to about 370 kW due to flow reactivity effects. At approximately 20 seconds, colder fuel salt arrives in the reactor which contributes positive reactivity. Temperature effects dominate the core power response to the remainder of the transient. The mass flow rate more than doubles in a short period of 40 seconds and decays to about 1 kg/sec after a period of approximately 10 minutes concomitant with reactor shutdown. Severe power rates do result in significant system temperature transients which contribute to high thermal stresses particularly during cooldown transient where stresses are more limiting to the reactor vessel structures. As expected, the heat exchanger has the coldest system temperatures and severe power transient can challenge both fuel salt solubility (approximately 550°C for 18 mol% UF_4) and solidus conditions (freezing temperature of approximately 453°C) of the fuel in local regions. For this reason, active control systems must be used to mitigate the severity of such transients.

These models assume adiabatic conditions at system fluid boundaries (no internal structure conduction, for instance) and no decay generation upon loss of heat sink accidents. The adiabatic assumption may need be conservative from a safety perspective in some cases. While the adiabatic assumption pro-

vides a lower bounding temperature case for heat sink surfaces (particularly near low, inner surfaces), the heat losses to the environment combined with thermal conduction of heat across the downcomer control volume may or may not promote natural circulation depending on net heat flux conditions in the downcomer. A full thermal analysis is needed to determine net heat balance conditions in the system due to internal conduction and losses to the environment.

Fig. 6 illustrates a STAR-CCM+ simulation highlighting the effect of loss of heat sink followed by rapid restart. Initial system power is 400 kW stead state. At time zero the system experiences a prompt loss of heat sink for 1000 seconds (approximately 17 minutes). At time 1000 seconds, the system power demand increases rapidly to 1 MW. On loss of heat sink, initial core power peaks at approximately 422 kW due to flow reactivity effects. Maximum reactor outlet temperatures approach about 940 K. Upon reactor rapid startup at 1000 sec, core power reaches a minimum at approximately 1200 sec at about 388 kW before rising rapidly to a peak core power of approximately 3.8 MW. System mass flow rate response autonomously to the heat sink power demand. As in the python model, core reactivity is dominated by the temperature coefficient. Thermal transients in the heat exchanger are severe and must be evaluated in detail to ensure yield strength limitation are not approached at temperatures above the reference transition temperatures of the material involved in the design (316 SS in this case).

A comparison of simulated results between the author's Python code and STAR-CCM+ for a 400 to 800 kW power demand transient response are shown in Fig. 7. The Python code generally provides a faster power response with reduced power overshoots and faster power damping than the CFD code in STAR-CCM+. The physics code is the same in both codes and therefore differences can be attributed to the improved fidelity of the STAR-CCM thermal-hydraulic computations. While it is ideally desirable to use a coupled multi-physics simulations using STAR-CCM+ to accomplish detailed studies to MSR transient response, this approach can be computationally expensive as each 2400 sec real time simulation can take up to a week using 40 cores on a HPC system. By contrast, a Python code simulation on a work station can provide results in under an hour total run time.

4 Results

4.1 Power Demand Transients

The total flow loop length is 5.71 meters. For nominal evaluated flow rates, the fuel salt loop transport time is about 115 seconds or 1.9 minutes. This causes transient system response to take several loop transport cycle times to stabilize. Simulations show that quasi-steady state conditions following power demand changes can be achieved in about 40 minutes. Initial conditions are assigned in the code based on an analytical estimate of steady state conditions in the closed-loop system. A simplified natural circulation, closed-loop system is illustrated in Fig.8. Any offsets to actual system steady state conditions introduce an initial run time transient. This transient takes the standard time to "ring down" until numerical steady state system values are used by the code. This initial "ring down" time can be minimized by adjusting initial conditions to match the numerically derived steady state values. This process allows the code to settle on steady state values in the shortest possible time. For this reason, it

is always a good practice to run the code for a minimum of 25,000 runtime seconds to ”ring out” any transients that may be in the numerical calculations and ensure results more accurately reflect transient being investigated. The initial spatial temperature profile is shown in Fig.9. The initial temperature rise is due to reactor heating which is assumed linear throughout the core. The system is assumed to be adiabatic and therefore temperatures do not change between system heat source and heat sink. At each time step, the reactor and heat exchanger outlet temperatures are spatially advanced by a distance proportional to the salt flow rate. In this way, outlet temperatures arrive at the downstream inlet at the proper time. Updated outlet temperatures are calculated at each time step based on time updated reactor power and heat exchanger power demand. Hot and cold leg densities that drive salt flow are calculated based on a spatial-averaged density value at each time step. In addition to density, time step propagated local temperatures are used to calculate updated specific heats, flow driving differential pressure, mass flow rate, and core reactivities.

Under certain conditions, the system is unstable and may experience flow instabilities or un-damped flow oscillations or reversals due to density inversions in the hot and leg legs of the loop. Flow reversals were noted during specifically design transients that challenged the inherent system temperature and flow feedback. Detailed evaluation of instabilities is left for future study and not addressed in this paper. Further investigation is recommended so that designs can be modified to accommodate, mitigate, and eliminate instabilities during power operations. Future work may support safety basis engineering analysis prior to fielding a design for demonstration for both natural and forced circulation flow modes.

Unless otherwise stated, this investigation was completed using the parameters provided in Table 1. Table 1 neutronic values were obtaining using Serpent 2.1.31 particle transport code on the micro-volume molten salt nuclear battery design. Flow reactivity coefficients were derived using prior numerical work by Dulla (Dulla, 2005).

4.2 MSR Compound Dynamic Effect

Figs.10 through 13 illustrate Python model results for a power demand transient between 250 kW to 1000 kW steady-state. Fig.10 depicts the Fourier transform of the reactivity components in the frequency domain. Both temperature and flow components have maximum amplitudes at low frequencies. This is expected due to the loop transport time (115 sec). This implies a natural response frequency of about 0.01 Hz. Across the spectrum of frequencies shown in Fig.10, the flow component leads the temperature component by π radian. This is expected, since the flow component is driven by global density variations in the hot and cold loop segments whereas the temperature component is a local function of core temperature.

Figs.11 through 13 are phase space diagrams from both up-power and down-power transients. The blue curves represent the transient from 250kW to 1000kW and the red curve represents power change from 1000kW to 250kW. Power-Velocity transitions tend to closely follow geodesic trajectories between initial and final state. Reactivity-Velocity trajectories tend to be less constrained because core reactivity changes do not linearly result in system flow changes. This is can be seen in the flat (horizontal) trajec-

tories near initial and final state points. Temperature-Flow reactivity trajectories both begin at the origin. Again, approach trajectories to final state tend to involve flat (horizontal) approach due to insensitivity of the flow component.

5 Future work

Specific recommended work to follow-up on this study might include:

- Use of STAR-CCM+ to model time dependent MSR behavior in a full scale 3D form is novel work. Future work to complete a thermal-physical analysis of system performance to characterize proximity to freezing and solubility is essential work in support of safety studies.
- Evaluation of potential design basis casualties under limiting power transient conditions.
- Evaluate for the bounding power transient safety case that inserts the maximum credible instability into the system.

Literature review indicates little prior work has been completed in the area of MSR power transient behavior especially in the area of natural circulation. This is a rich field for research and will help inform MSR safety basis analysis in support of concept demonstration and commercial licensing.

6 Summary

A time-dependent, finite-element python code was developed to model the MSR power transient behavior in natural circulation flow using modified one-group kinematics adapted to the MSR system. The modified kinematics involve consideration of a fuel saly velocity dependent effective delayed neutron fraction. Opposing reactivity effects associated with flow velocity and temperature act on changing reactor power. Flow related neutronics effects cause reactor power to decrease initially after a up-power demand from the heat exchanger. Likewise, reactor power increases initially on down-power demands. This is unique to MSR systems and counter to traditional lead-follow heat balance systems. Python code results were compared to STAR-CCM+ simulations using equivalent physics models. Comparisons were found to be similar and reasonable for the purposes of rudimentary thermal-hydraulic analysis especially in light of the considerable computational savings afforded. Results show that the natural circulation MSR system does exhibit critical damped characteristics. Further work using equivalent approaches to the python code or full 3D CFD simulations using STAR-CCM+ like CFD tools, for instance, is of interest to help fully characterize time-dependent MSR performance under nominal and off-nominal scenarios. Proximity to fuel salt solubility and themral-physical constraints are of specific interest to develop mature accident tolerant MSR designs.

The flow reactivity coefficient is unique to MSRs and is strongly dependent system geometry and fuel salt flow velocity. Forced circulation MSR designs with constant flow do not have strong flow components. Natural circulation operating regimes or loss of force flow accident scenarios makes this

technical analysis important to safety basis development for all MSRs. This opens a rich area for engineering inputs that can affect core performance outcomes.

Abbreviations

BWR	Boiling Water Reactor
CDE	Compound Dynamic Effect
CFD	Computational Fluid Dynamics
DNP	Delayed Neutron Precursors
FLiNaK	Flouride Lithium Sodium Potassium Salt
GIF	Generation IV International Forum
HALEU	High Assay Low Enriched Uranium
HFIR	High Flux Isotope Reactor
HPC	High Performance Computing
IAEA	International Atomic Energy Agency
IMSR	Integral Molten Salt Reactor
LWR	Light Water Reactor
MSFR	Molten Salt Fast Reactor
MsNB	Molten Salt Nuclear Battery
MSR	Molten Salt Reactor
MSRE	Molten Salt Reactor Experiment
PLC	Pressure Loss Coefficient
PWR	Pressurized Water Reactor
TRU	Transuranic

Constants and Symbols

ϕ_o	Static neutron flux ($\mathrm{cm}^{-2}\ \mathrm{s}^{-1}$)
β_{eff}	Effective Delayed Neutron Precursor fraction
λ	One-group delayed neutron precursor decay constant (sec^{-1})
C_o	Static Delayed Neutron Precursor concentration (cm^{-3})
u_o	Static molten salt fuel flow velocity (cm s^{-1})
a	Core half height (cm)
τ	Reactor Period (sec)
H	Core length (cm)
L	External core loop length (cm)
P	Pressure (Pa)
ρ	Density (kg m^{-3})
g	Gravitational Constant
$v_{\mathrm{in/out}}$	Flow velocity (cm s^{-1})
$\bar{v}$	Average fuel salt flow velocity (cm s^{-1})
ξ	Pressure Loss Coefficient
$h_{\mathrm{in/out}}$	Fluid specific enthalpy (J kg^{-1})
h	Distance between thermal centers (cm)
f	Darcy friction factor
D_H	Hydraulic diameter (cm)
K	Hydraulic loss factor
$\dot{Q}$	Heat production rate (W)
$\dot{m}$	Mass flow rate (kg s^{-1})
c_p	Specific heat capacity (J $\mathrm{kg}^{-1}\ \mathrm{K}^{-1}$)
$T_{\mathrm{in/out}}$	Temperature (K)
w_i	Weight percent fraction
α_T	Temperature coefficient of reactivity (pcm K^{-1})
α_f	Flow reactivity exponent (sec cm^{-1})
ρ_f	Reactivity due to flow (pcm)
ρ_T	Reactivity due to temperature (pcm)
ρ_∞	Flow reactivity at infinite flow velocity (pcm)
K_{eff}	Neutron multiplication factor
$f(u)$	Precursor fraction function
l^*	Prompt neutron lifetime (sec)
Pe	Peclet number
k	Thermal conductivity (J $\mathrm{m}^{-1}\ \mathrm{K}^{-1}$)

7 Table

Table 1: Model Thermal and Neutronics Parameters

Parameter	
α_T (pcm/K)	-3.5
l^* (sec)	1.63 x 10^{-4}
β	6.96 x 10^{-3}
λ (sec)	0.1
h (m)	1.09
ξ	25.0
α_f (s/cm)	3.3976917 x 10^{-1}
dt (sec)	1.0
dx (cm)	1.0

Table 2: MsNB Reactor Integrated Path Linear Dimensions

Parameter	**Path Length (cm)**
Reactor Inlet	0.0
Reactor Outlet	166.0
Loop Top Height	209.0
Heat Exchanger (Hx) Inlet	234.0
Hx Loop Top	282.5
Hx Outlet	282.5
Loop Bottom	497.5
Reactor Inlet	571.0

8 Figures

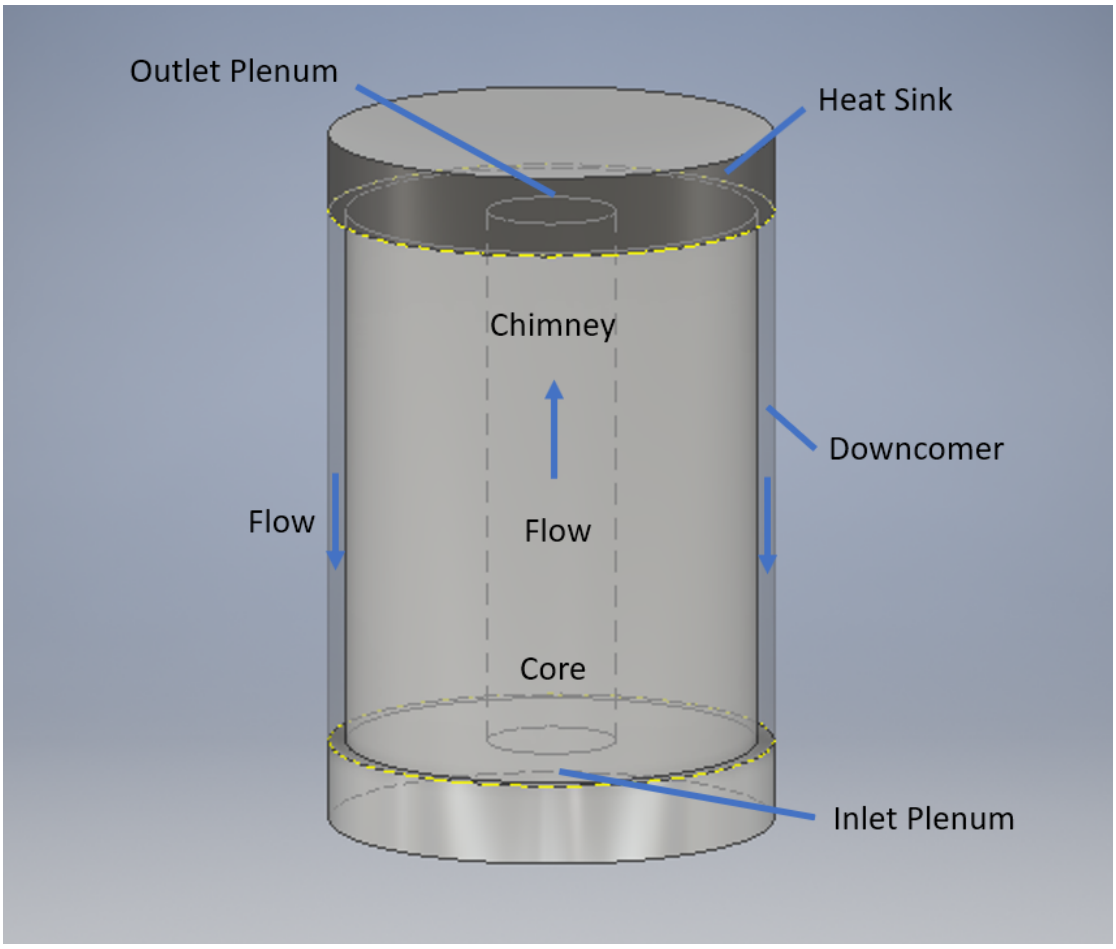

Figure 1: Axial cross section diagram of the FLiNaK molten salt nuclear battery. Flow propagates vertically up through the core and chimney, enters the outlet plenum, flows radially out through the heat exchanger, downward through the downcomer, collects below the core in the inlet plenum, and repeats the flow cycle. Total loop linear flow distance is 571 cm. Nominal transport time is 130 seconds. (Cardenas Melgar, 2021).

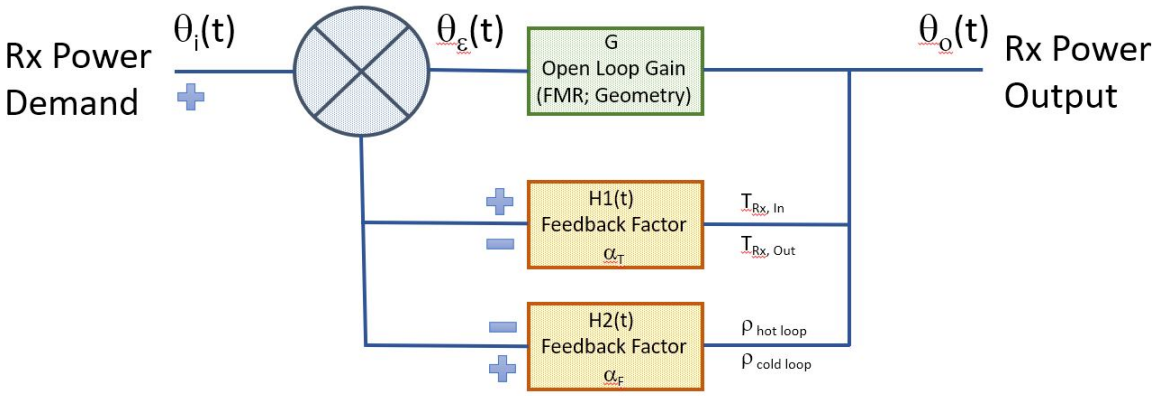

Figure 2: Compound Dynamic Power Control of a Natural Circulation Molten Salt Reactor System. Compound time-delayed feedback factors make the MSR power control system unique. In natural circulation modes of operation, the time-dependent flow reactivity feedback factor (H2) is a significant contribution to power response behavior and defines transitions to instabilities such as flow oscillations and reversals.

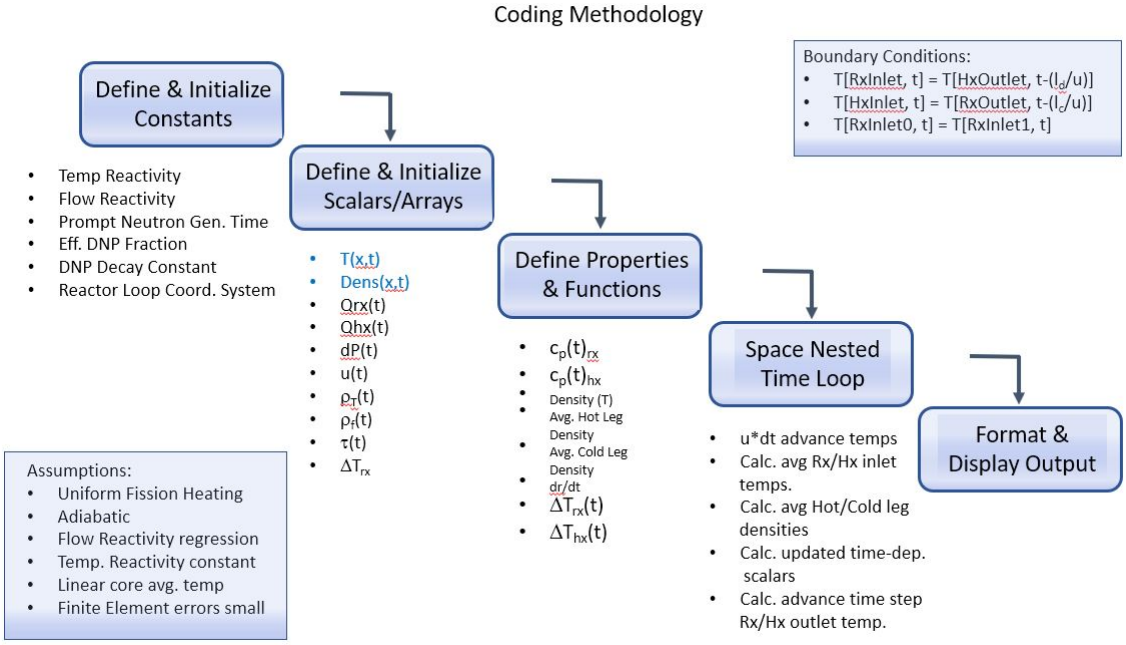

Figure 3: Coding Methodology.

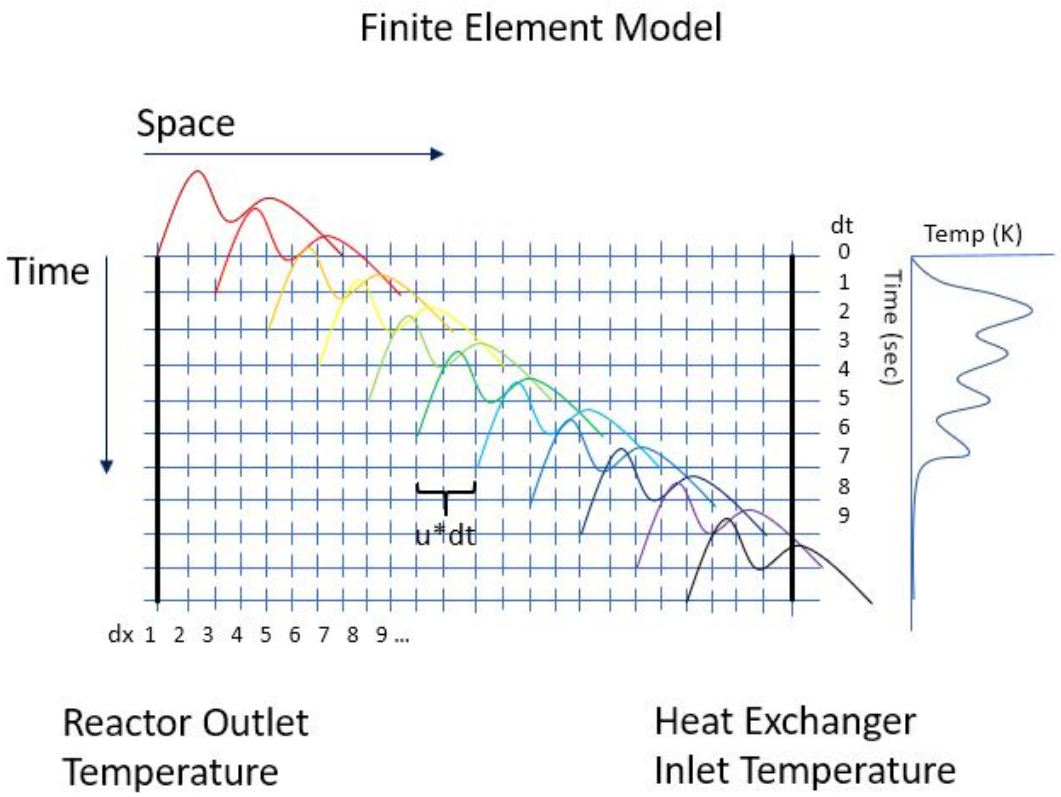

Figure 4: Finite Element Approach.

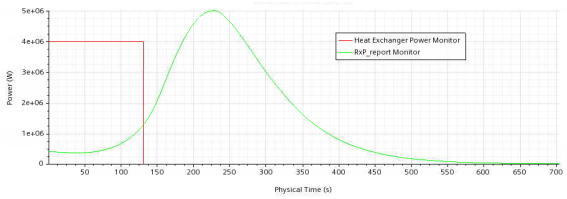

(a) Reactor and Heat Exchanger Power

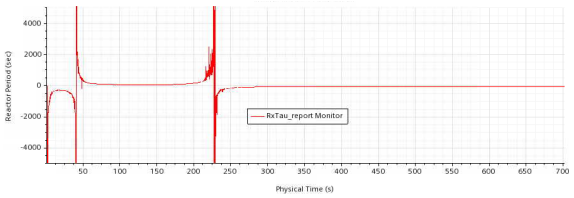

(b) Reactor Period

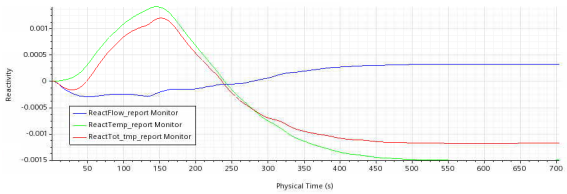

(c) Core Reactivity

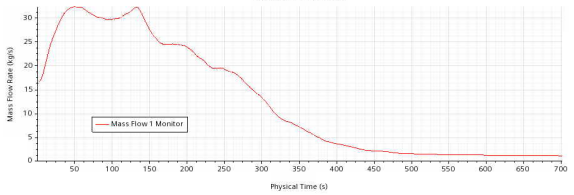

(d) Mass Flow Rate

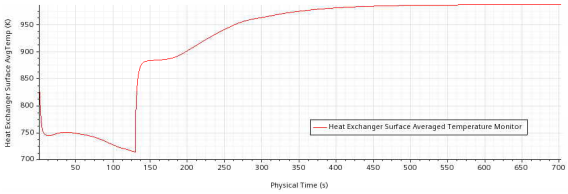

(e) Heat Exchanger Average Surface Temperature

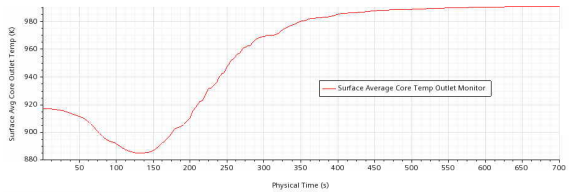

(f) Reactor Outlet Surface Averaged Temperature

Figure 5: STAR-CCM+ simulation showing overpower demand followed by loss of heat sink. Initial system power is 400 kW stead state. At time zero, the system experiences a prompt power demand increase to 4 MW for a duration of 130 seconds which corresponds to the time needed for flow reactivity dominance to subside. At time 130 seconds, the system power demand decreases to 0 kW. The initial reactor power response decreases to about 370 kW due to flow reactivity effects. At approximately 20 seconds, colder fuel salt arrives in the reactor which contributes positive reactivity. Temperature effects dominate the core power response to the remainder of the transient. The mass flow rate more than doubles in a short period of 40 seconds and decays to about 1 kg/sec after a period of approximately 10 minutes concombinate with reactor shutdown. Severe power rates do result in significant system temperature transients which contribute to high thermal stresses particularly during cooldown where stresses can be significantly limiting to thick walled the reactor vessel structures. As expected, the heat exchanger has the coldest system temperatures and severe power transient can challenge both fuel salt solubility (approximately 823 K for 18 mol% UF_4) and solidus conditions (freezing temperature of approximately 726 K) of the fuel in local regions (see fig. (e)). For this reason, active control systems must be used to mitigate the severity of such transients.

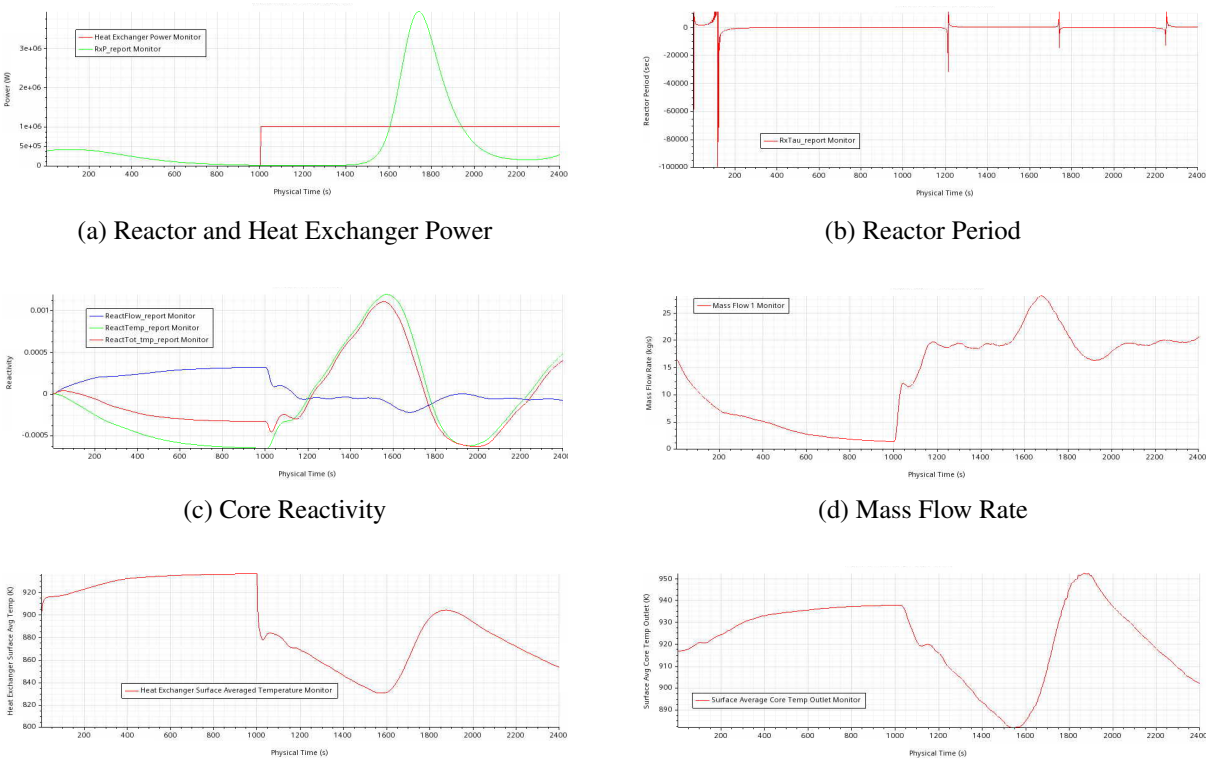

(a) Reactor and Heat Exchanger Power

(b) Reactor Period

(c) Core Reactivity

(d) Mass Flow Rate

(e) Heat Exchanger Average Surface Temperature

(f) Reactor Outlet Surface Averaged Temperature

Figure 6: STAR-CCM+ simulation showing effect of loss of heat sink followed by rapid restart. Initial system power is 400 kW stead state. At time zero the system experiences a prompt loss of heat sink for 1000 seconds (approximately 17 minutes). At time 1000 seconds, the system power demand increases rapidly to 1 MW. On loss of heat sink, initial core power peaks at approximately 422 kW due to flow reactivity effects. Maximum reactor outlet temperatures approach about 940 K. Upon reactor rapid startup at 1000 sec, core power reaches a minimum at approximately 1200 sec at about 388 kW before rising rapidly to a peak core power of approximately 3.8 MW. System mass flow rate response autonomously to the heat sink power demand. As in the python model, core reactivity is dominated by the temperature coefficient. Thermal transients in the heat exchanger are severe and must be evaluated in detail to ensure yield strength limitation are not approached at temperatures above the reference transition temperatures of the material involved in the design (316 SS in this case).

Figure 7: Comparison of simulated results for a 400 to 800 kW power demand transient response. The Python code generally provides a faster power response with reduced power overshoots and faster power damping than the CFD code in STAR-CCM+. The neutronics are the same in both codes and therefore differences can be attributed to the improved fidelity of the STAR-CCM thermal-hydraulic computations.

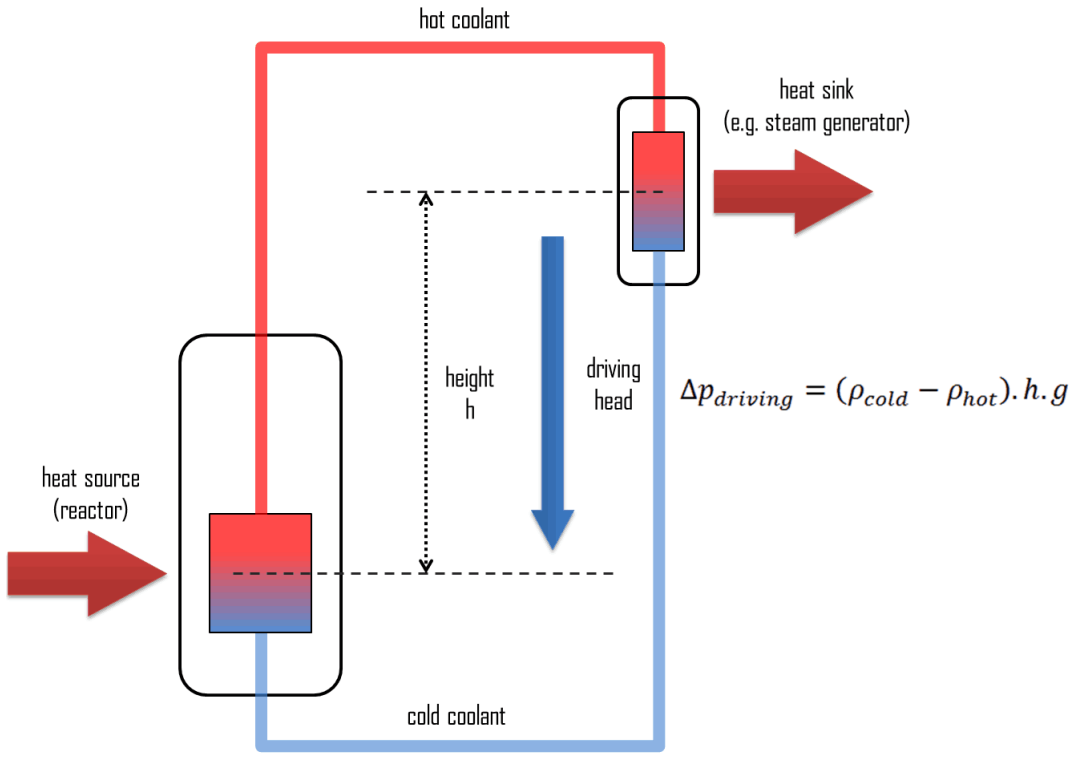

Figure 8: Simplified Natural Convection Closed Loop System. (IAEA, 2005)

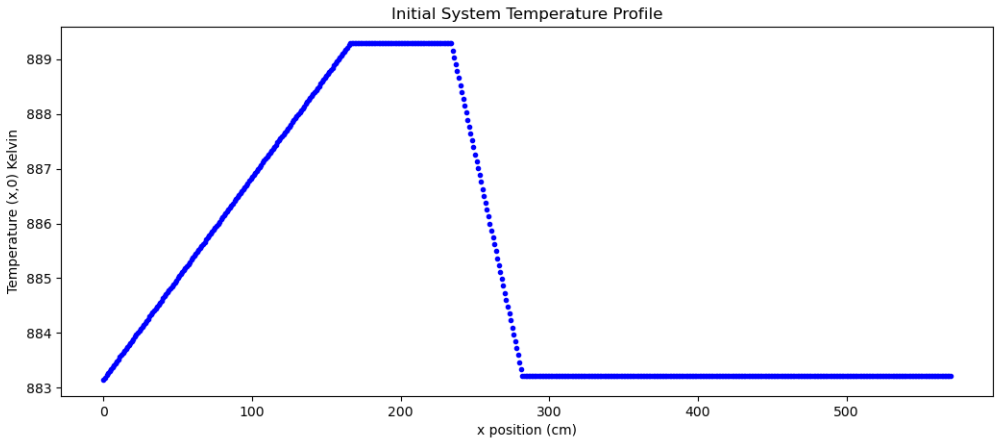

Figure 9: Initial reactor loop temperature profile. Nominal differential temperature across the reactor at 400 kWth power operation is about 5 degree Celsius. Heat generation and removal are assumed to be linear within the reactor and heat exchanger. The reactor thermodynamic control volume is assumed to be adiabatic and no preheating occurs in the downcomer flow region.

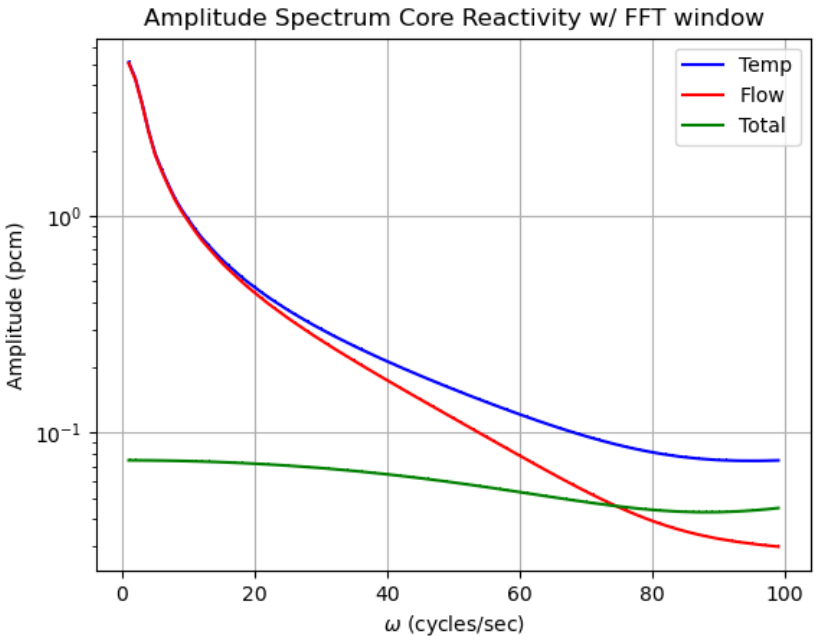

Figure 10: Stable Power Transient from 250 kW to 1000 kW over 10 minutes. Fast Fourier Transform of reactivity components. At low frequencies the temperature and flow reactivity components are out of phase. As frequency increases, the temperature component becomes the dominant contributor to overall core power behavior.

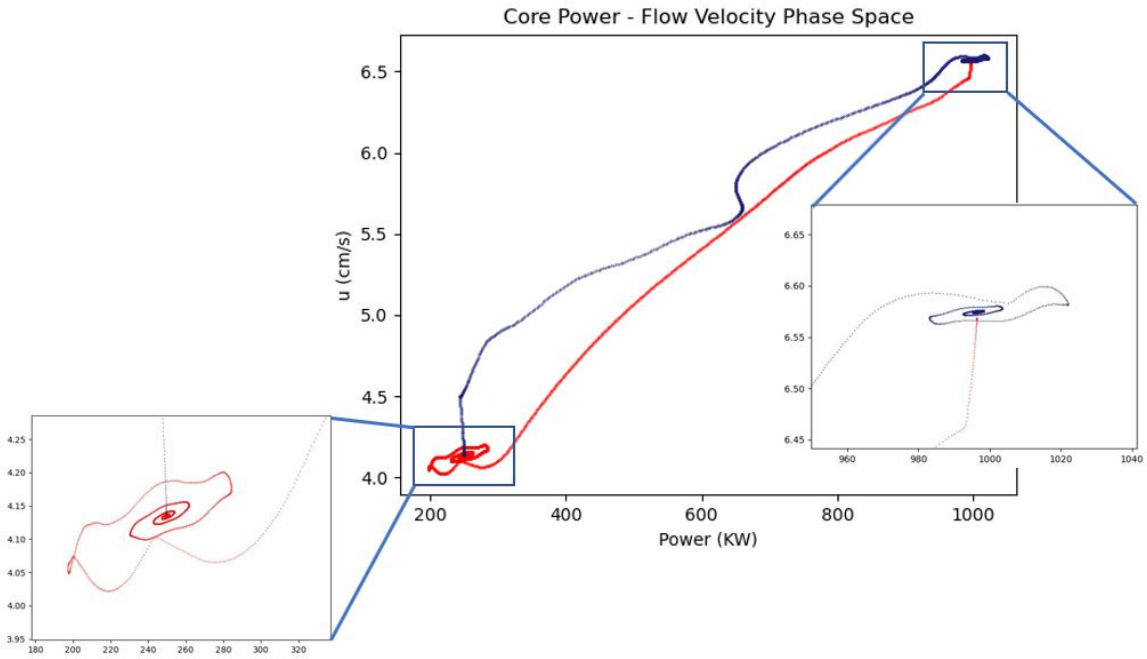

Figure 11: Power - Velocity phase space representation of a stable power transient. Up-power transient from 250 kW to 1000 kW indicated in blue. Down-power transient from 1000 kW to 250 kW indicated in red.

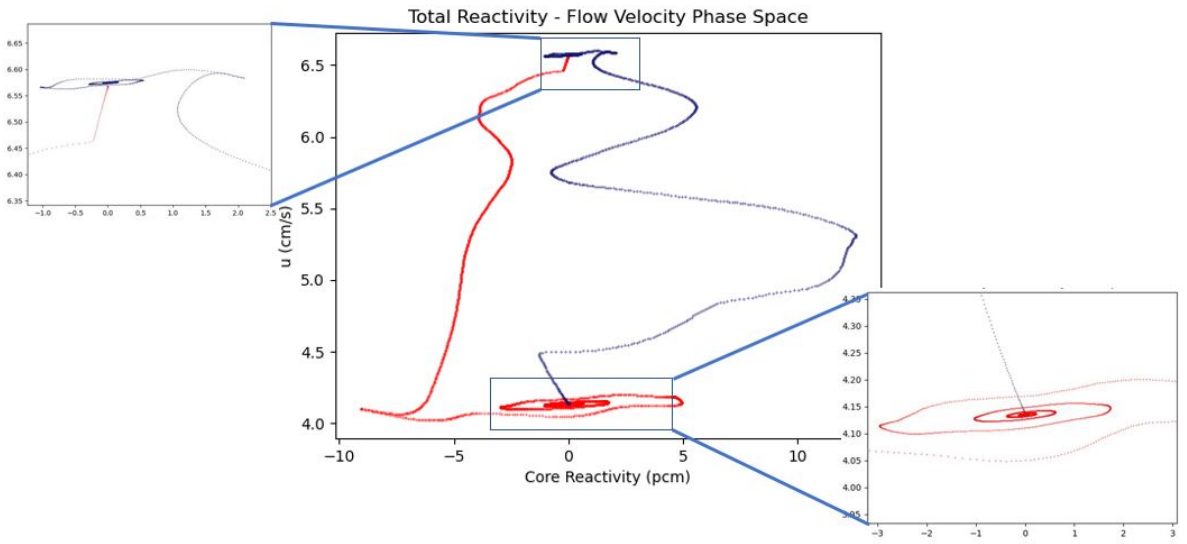

Figure 12: Reactivity - Velocity phase space representation of a stable power transient. Up-power transient from 250 kW to 1000 kW indicated in blue. Down-power transient from 1000 kW to 250 kW indicated in red.

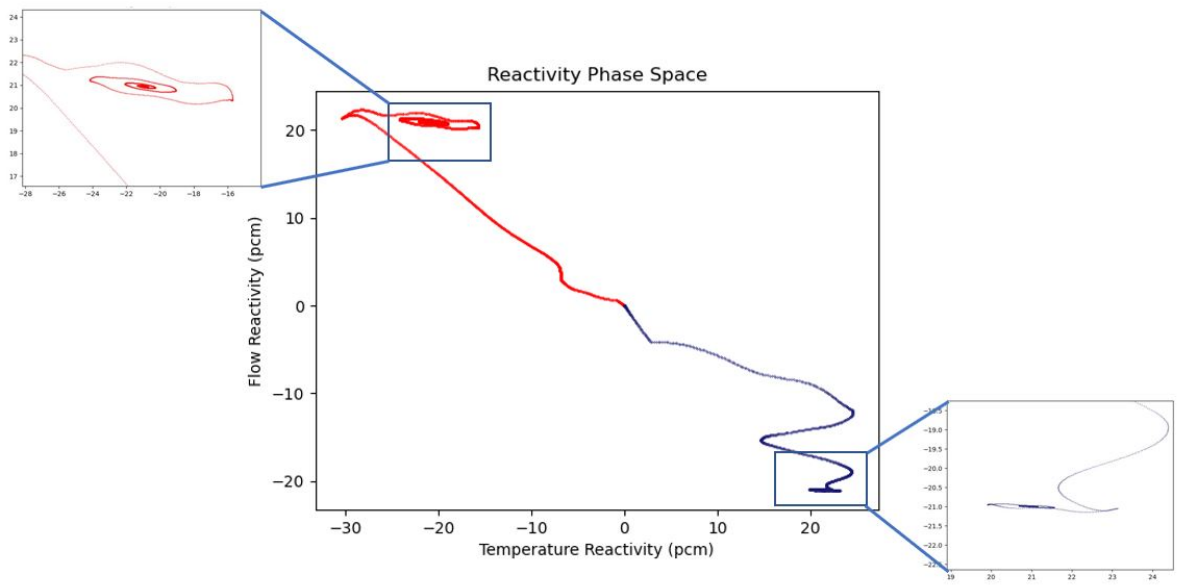

Figure 13: Temperature - Flow Reactivity phase space representation of a stable power transient. Up-power transient from 250 kW to 1000 kW indicated in blue. Down-power transient from 1000 kW to 250 kW indicated in red.

References

[1] Ambrosini W., et al, 1998. NUMERICAL ANALYSIS OF SINGLE-PHASE, NATURAL CIRCULATION IN A SIMPLE CLOSED LOOP, Dipartimento di Construzioni Meccaniche e Nucleari, Universitá di Pisa.

[2] Aufiero M., et al, 2014. Calculating the effective delayed neutron fraction in the Molten Salt Fast Reactor: Analytical, deterministic and MOnte Carlo approaches, Annals of Nuclear Energy 65, 78-90.

[3] Cardenas-Melgar A., et al, 2021. Report on the Friction Factor for the Offset-Strip Fin Heat Exchanger", unpublished manuscript.

[4] Carter J., Borrelli R., 2020a. Integral molten salt reactor neutron physics study using Monte Carlo N-particle code, Nuclear Engineering and Design, Vol. 365, 110718.

[5] Carter J., Borrelli R., 2020b. Integral molten salt reactor temperature sensitivities using Serpent target motion sampling, Nuclear Engineering and Design 369, 110863.

[6] Dass A., et al, 2021. Stability analysis of a single-phase rectangular Coupled Natural Circulation Loop system employing a Fourier series based 1-D mode", retrieved from https://arxiv.org/abs/2012.11003 on 14 June 2021.

[7] Desrayaudi G., et al, 2005. Steady and unsteady natural circulation in a single-phase 2D-annular loop, Proceedings of the 3rd IASME/WSEAS Int. Conf. on HEAT TRANSFER, THERMAL ENGINEERING AND ENVIRONMENT, Corfu, Greece.

[8] Desrayaudi, G., et al, 2013. Two-dimensional numerical analysis of a rectangular closed-loop thermosiphon, Appl. Therm. Eng. 50: 187-196.

[9] Dolan, 2017. Molten Salt Reactors and Thorium Energy, Woodhead Publishing.

[10] Duderstadt, James, J., 1976. Nuclear Reactor Analysis, John Wiley & Sons, Inc.

[11] Dulla S., 2005. Models and methods in the neutronics of fluid fuel reactors", Ph.D. Thesis, University of Torino, Italy.

[12] Guifeng, Z., 2019. Low enriched uranium and thorium fuel utilization under once-through and offline reprocessing scenarios in small modular molten salt reactor, International Journal of Energy Research 43(2).

[13] IAEA, 2005. Natural circulation in water cooled nuclear power plants, IAEA-TECDOC-1474. ISBN 92–0–110605–X. Image retrieved from https://www.nuclear-power.net/nuclear-engineering/heat-transfer/convection-convective-heat-transfer/natural-convection-free-convection/natural-circulation/ on 12 April 2021.

[14] IAEA, 2005. Natural circulation in water cooled nuclear power plants, IAEA-TECDOC-1474.

[15] International Atomic Energy Agency (IAEA), 2013. Challenges Related to the Use of Liquid Medal and Molten Salt Coolants in Advanced Reactors, IAEA-TECDOC-1696.

[16] Janna, W., 1998. Design of Fluid Thermal Systems, 2nd Ed, PWS Publishing Co.

[17] Lamarsh, John R., 2001. Introduction to Nuclear Engineering, 3rd Edition, Addison-Wesley Company.

[18] Lizin, A., 2013. UF4, ThF4 SOLUBILITY IN LiF–NaF–KF MELT, Atomic Energy, Vol. 115, No. 1 (Russian Original Vol. 115, No. 1, July 2013).

[19] Manohar S. Sohal, et. al., 2013. Engineering Database of Liquid Salt Thermophysical and Thermochemical Properties, INL/EXT-10-18297 Rev.1.

[20] Nayak, A.K., 1995. Mathematical modelling of the stability characteristics of a natural circulation loop, Math. Comput. Model. 22: 77-87.

[21] Nayak, A.K., et al, 2009. Thermal-hydraulic characteristics of a single-phase natural circulation loop with water and Al_2O_3 nanofluids, Nucl. Eng. Des. 239: 526-540.

[22] Pazsit, I., 2017. Kinetics and dynamics (including noise analysis) of Molten Salt Reactors, microsoft power point from Chalmers University of Technology.

[23] Pini A., et al, 2016. Analytical and numerical investigation of the heat exchange effect on the dynamic behaviour of natural circulation with internally heated fluids, Chem. Eng. Sci. 145: 108-125.

[24] Sabharwall, P., Yoo, Y., Wu Q., Sienicki, J., 2012. Natural Circulation and Linear Stability Analysis for Liquid-Metal Reactors with the Effect of Fluid Axial Conduction, Nuclear Technology, vol 178.

[25] Saha R., et al, 2018. Flow reversal prediction of a single-phase square natural circulation loop using symbolic time series analysis, International Conference on Mechanical Engineering held at Jadavpur University, Kolkata, India during January 4–6.

[26] Serrano-Lopez R., Fradera J., Cuesta-Lopez S., 2013. Molten Salts Database for Energy Applications, Chemical Engineering and Processing: Process Intensification, Universidad de Burgos, Spain.

[27] Siemens Digital Industries Software, 2020, " Simcenter STAR-CCM+ Documentation version 2020.3, Product Overview and User Guide", *www.siemens.com/mdx*

[28] Watanabe N., et al, 2008. Thermal Hydraulic Flow Oscillation Characteristics in Multiformed Channels under Natural Circulation and Low-Pressure Conditions, Journal of Nuclear Science and Technology, 45:2, 160-170, DOI: 10.1080/18811248.2008.9711425.

[29] Welander P., 1967. On the oscillatory instability of a differentially heated fluid loop. J. Fluid Mech. 29(1).

[30] Vijayan P.K., 2010. Joint ICTP-IAEA Course on Natural Circulation Phenomena and Passive Safety Systems in Advanced Water Cooled Reactors, International Center for Theoretical Physics, No. 2152-22.

[31] Zou L., et al, 2017. Numerical study on the Welander oscillatory natural circulation problem using high-order numerical methods, Progress in Nuclear Energy 94, 162-172.

Declaration of interests

☒ The authors declare that they have no known competing financial interests or personal relationships that could have appeared to influence the work reported in this paper.

☐ The authors declare the following financial interests/personal relationships which may be considered as potential competing interests:

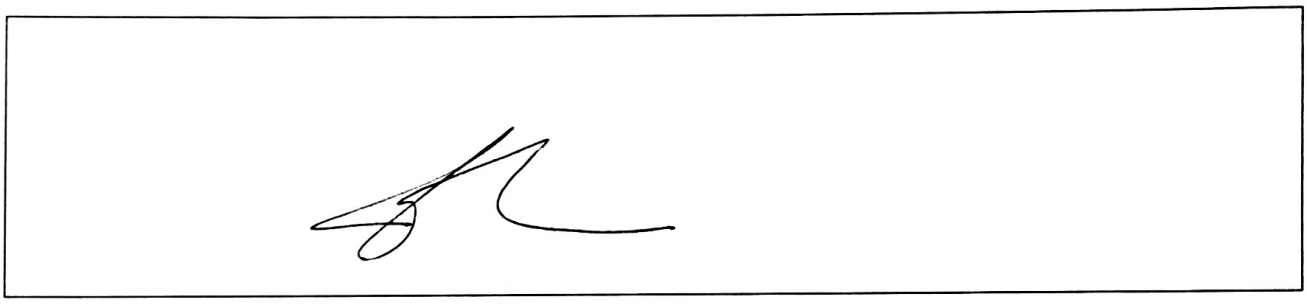

Credit Author Statement

John P. Carter: Conceptualization, Methodology, Software, Formal Analysis, Resources, Data Curation, Writing – Original Draft, Writing- Review & Editing, Visualization. **Richard Christensen:** Writing-Review & Editing, Supervision. **SuJong Yoon**: Methodology, Software, Writing-Review & Editing.

References

[1] Ambrosini W., et al, 1998. NUMERICAL ANALYSIS OF SINGLE-PHASE, NATURAL CIRCULATION IN A SIMPLE CLOSED LOOP, Dipartimento di Construzioni Meccaniche e Nucleari, Universitá di Pisa.

[2] Aufiero M., et al, 2014. Calculating the effective delayed neutron fraction in the Molten Salt Fast Reactor: Analytical, deterministic and MOnte Carlo approaches, Annals of Nuclear Energy 65, 78-90.

[3] Cardenas-Melgar A., et al, 2021. Report on the Friction Factor for the Offset-Strip Fin Heat Exchanger", unpublished manuscript.

[4] Carter J., Borrelli R., 2020a. Integral molten salt reactor neutron physics study using Monte Carlo N-particle code, Nuclear Engineering and Design, Vol. 365, 110718.

[5] Carter J., Borrelli R., 2020b. Integral molten salt reactor temperature sensitivities using Serpent target motion sampling, Nuclear Engineering and Design 369, 110863.

[6] Dass A., et al, 2021. Stability analysis of a single-phase rectangular Coupled Natural Circulation Loop system employing a Fourier series based 1-D mode", retrieved from https://arxiv.org/abs/2012.11003 on 14 June 2021.

[7] Desrayaudi G., et al, 2005. Steady and unsteady natural circulation in a single-phase 2D-annular loop, Proceedings of the 3rd IASME/WSEAS Int. Conf. on HEAT TRANSFER, THERMAL ENGINEERING AND ENVIRONMENT, Corfu, Greece.

[8] Desrayaudi, G., et al, 2013. Two-dimensional numerical analysis of a rectangular closed-loop thermosiphon, Appl. Therm. Eng. 50: 187-196.

[9] Dolan, 2017. Molten Salt Reactors and Thorium Energy, Woodhead Publishing.

[10] Duderstadt, James, J., 1976. Nuclear Reactor Analysis, John Wiley & Sons, Inc.

[11] Dulla S., 2005. Models and methods in the neutronics of fluid fuel reactors", Ph.D. Thesis, University of Torino, Italy.

[12] Guifeng, Z., 2019. Low enriched uranium and thorium fuel utilization under once-through and offline reprocessing scenarios in small modular molten salt reactor, International Journal of Energy Research 43(2).

[13] IAEA, 2005. Natural circulation in water cooled nuclear power plants, IAEA-TECDOC-1474. ISBN 92–0–110605–X. Image retrieved from https://www.nuclear-power.net/nuclear-engineering/heat-transfer/convection-convective-heat-transfer/natural-convection-free-convection/natural-circulation/ on 12 April 2021.

[14] IAEA, 2005. Natural circulation in water cooled nuclear power plants, IAEA-TECDOC-1474.

[15] International Atomic Energy Agency (IAEA), 2013. Challenges Related to the Use of Liquid Medal and Molten Salt Coolants in Advanced Reactors, IAEA-TECDOC-1696.

[16] Janna, W., 1998. Design of Fluid Thermal Systems, 2nd Ed, PWS Publishing Co.

[17] Lamarsh, John R., 2001. Introduction to Nuclear Engineering, 3rd Edition, Addison-Wesley Company.

[18] Lizin, A., 2013. UF4, ThF4 SOLUBILITY IN LiF–NaF–KF MELT, Atomic Energy, Vol. 115, No. 1 (Russian Original Vol. 115, No. 1, July 2013).

[19] Manohar S. Sohal, et. al., 2013. Engineering Database of Liquid Salt Thermophysical and Thermochemical Properties, INL/EXT-10-18297 Rev.1.

[20] Nayak, A.K., 1995. Mathematical modelling of the stability characteristics of a natural circulation loop, Math. Comput. Model. 22: 77-87.

[21] Nayak, A.K., et al, 2009. Thermal-hydraulic characteristics of a single-phase natural circulation loop with water and Al_2O_3 nanofluids, Nucl. Eng. Des. 239: 526-540.

[22] Pazsit, I., 2017. Kinetics and dynamics (including noise analysis) of Molten Salt Reactors, microsoft power point from Chalmers University of Technology.

[23] Pini A., et al, 2016. Analytical and numerical investigation of the heat exchange effect on the dynamic behaviour of natural circulation with internally heated fluids, Chem. Eng. Sci. 145: 108-125.

[24] Sabharwall, P., Yoo, Y., Wu Q., Sienicki, J., 2012. Natural Circulation and Linear Stability Analysis for Liquid-Metal Reactors with the Effect of Fluid Axial Conduction, Nuclear Technology, vol 178.

[25] Saha R., et al, 2018. Flow reversal prediction of a single-phase square natural circulation loop using symbolic time series analysis, International Conference on Mechanical Engineering held at Jadavpur University, Kolkata, India during January 4–6.

[26] Serrano-Lopez R., Fradera J., Cuesta-Lopez S., 2013. Molten Salts Database for Energy Applications, Chemical Engineering and Processing: Process Intensification, Universidad de Burgos, Spain.

[27] Siemens Digital Industries Software, 2020, " Simcenter STAR-CCM+ Documentation version 2020.3, Product Overview and User Guide", *www.siemens.com/mdx*

[28] Watanabe N., et al, 2008. Thermal Hydraulic Flow Oscillation Characteristics in Multiformed Channels under Natural Circulation and Low-Pressure Conditions, Journal of Nuclear Science and Technology, 45:2, 160-170, DOI: 10.1080/18811248.2008.9711425.

[29] Welander P., 1967. On the oscillatory instability of a differentially heated fluid loop. J. Fluid Mech. 29(1).

[30] Vijayan P.K., 2010. Joint ICTP-IAEA Course on Natural Circulation Phenomena and Passive Safety Systems in Advanced Water Cooled Reactors, International Center for Theoretical Physics, No. 2152-22.

[31] Zou L., et al, 2017. Numerical study on the Welander oscillatory natural circulation problem using high-order numerical methods, Progress in Nuclear Energy 94, 162-172.

1 Table

Table 1: Model Thermal and Neutronics Parameters

Parameter	
α_T (pcm/K)	-3.5
l^* (sec)	1.63 x 10^{-4}
β	6.96 x 10^{-3}
λ (sec)	0.1
h (m)	1.09
ξ	25.0
α_f (s/cm)	3.3976917 x 10^{-1}
dt (sec)	1.0
dx (cm)	1.0

Table 2: MsNB Reactor Integrated Path Linear Dimensions

Parameter	**Path Length (cm)**
Reactor Inlet	0.0
Reactor Outlet	166.0
Loop Top Height	209.0
Heat Exchanger (Hx) Inlet	234.0
Hx Loop Top	282.5
Hx Outlet	282.5
Loop Bottom	497.5
Reactor Inlet	571.0

1 Figures

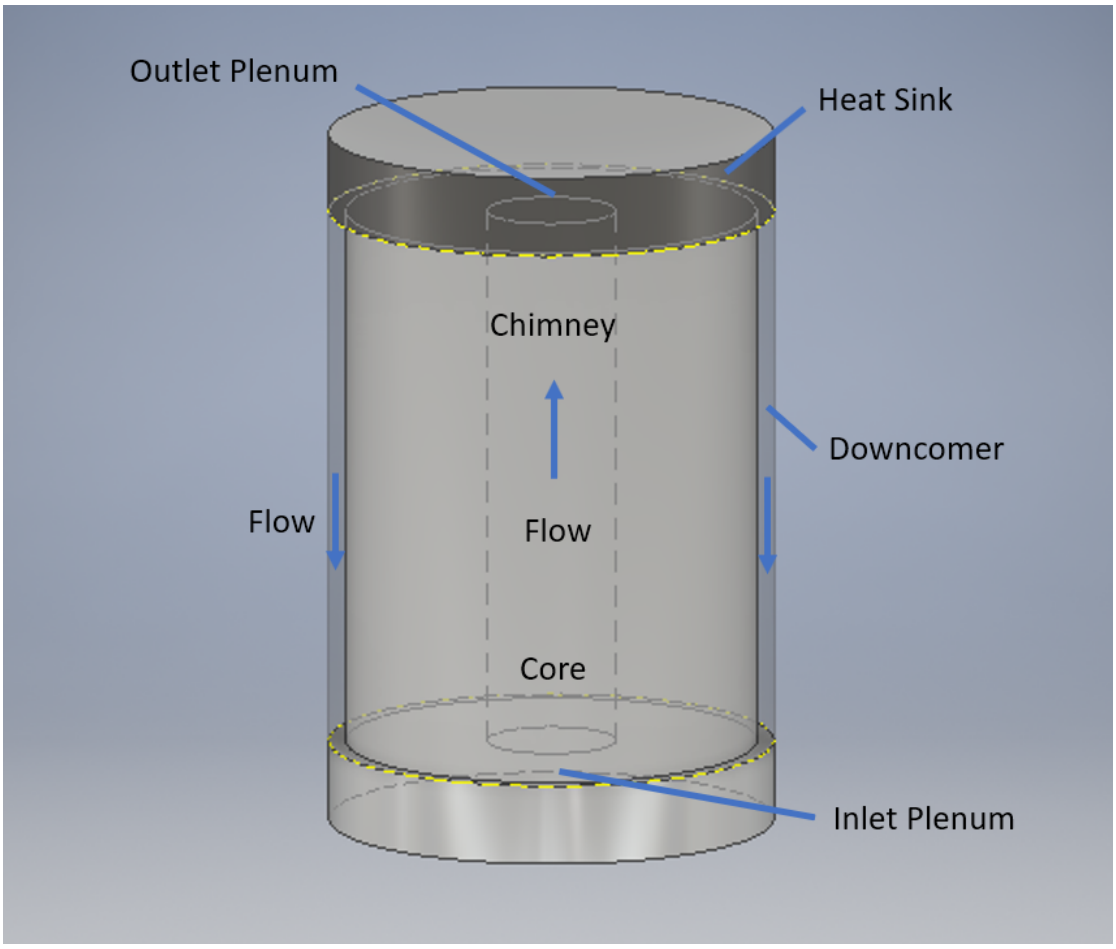

Figure 1: Axial cross section diagram of the FLiNaK molten salt nuclear battery. Flow propagates vertically up through the core and chimney, enters the outlet plenum, flows radially out through the heat exchanger, downward through the downcomer, collects below the core in the inlet plenum, and repeats the flow cycle. Total loop linear flow distance is 571 cm. Nominal transport time is 130 seconds. (Cardenas Melgar, 2021).

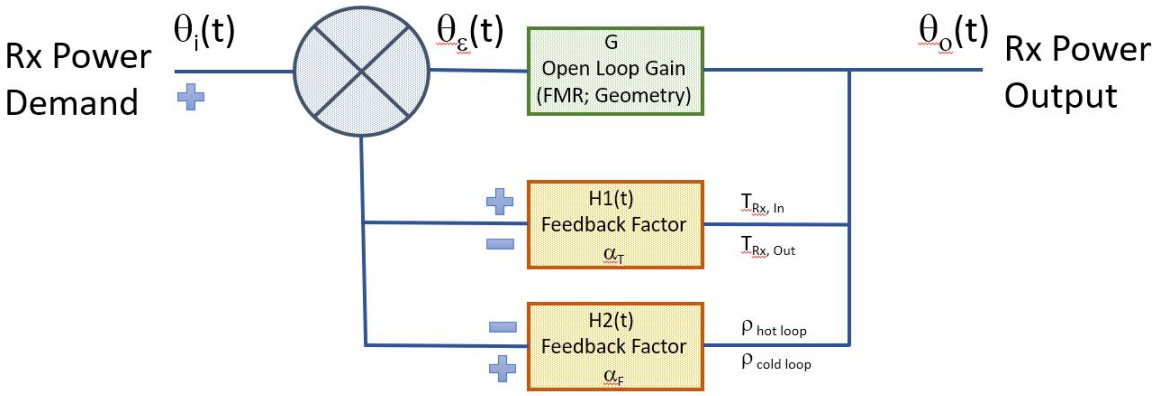

Figure 2: Compound Dynamic Power Control of a Natural Circulation Molten Salt Reactor System. Compound time-delayed feedback factors make the MSR power control system unique. In natural circulation modes of operation, the time-dependent flow reactivity feedback factor (H2) is a significant contribution to power response behavior and defines transitions to instabilities such as flow oscillations and reversals.

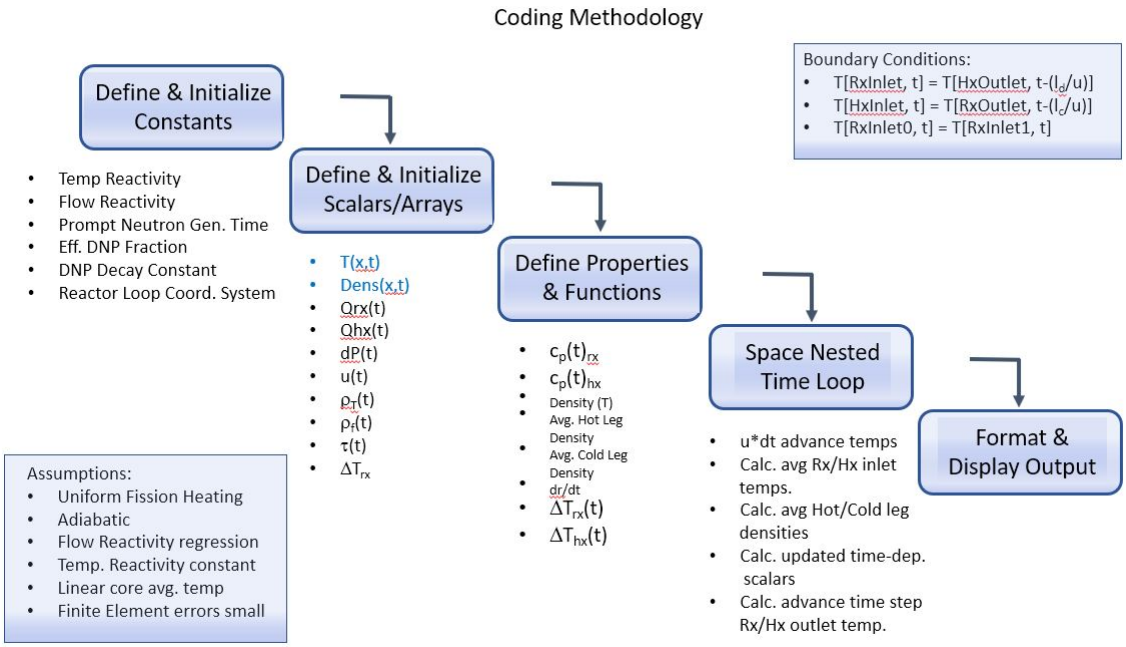

Figure 3: Coding Methodology.

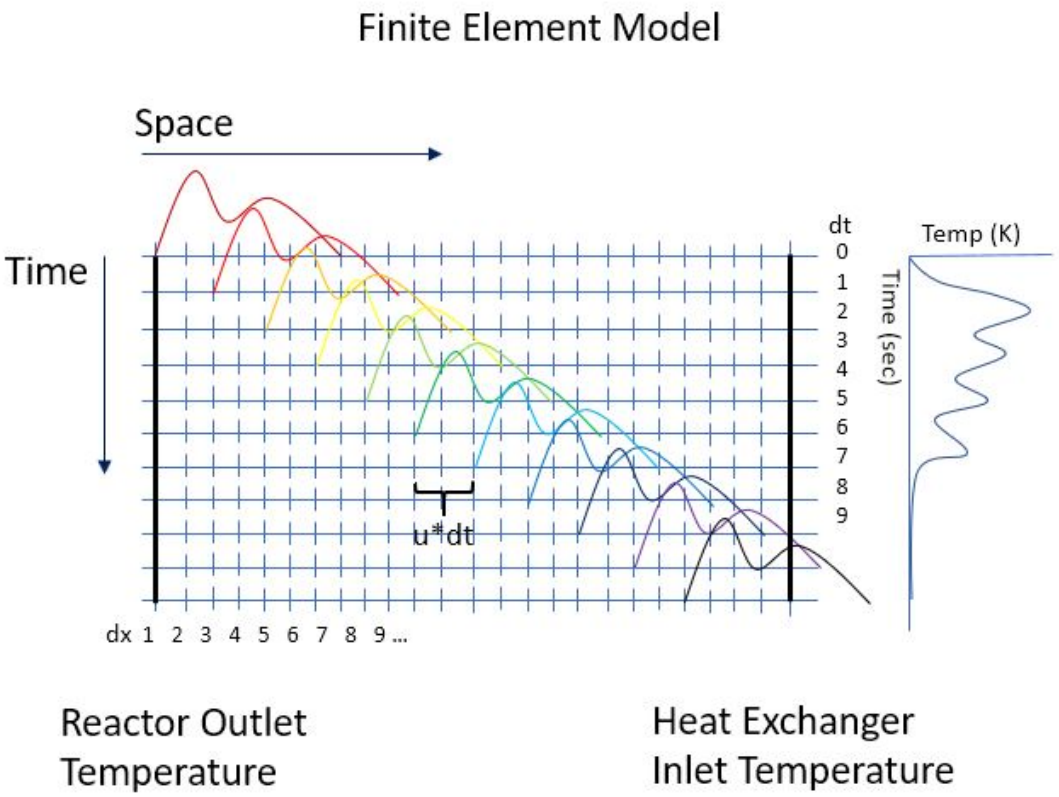

Figure 4: Finite Element Approach.

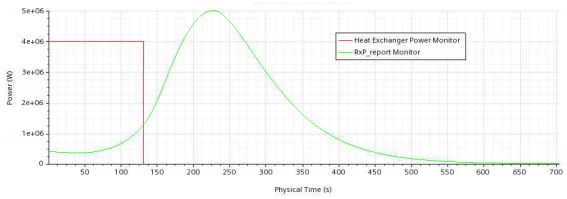

(a) Reactor and Heat Exchanger Power

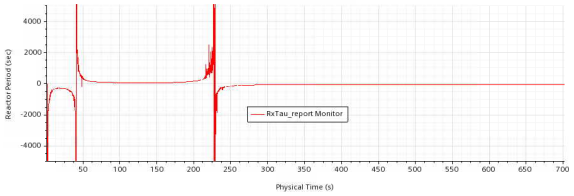

(b) Reactor Period

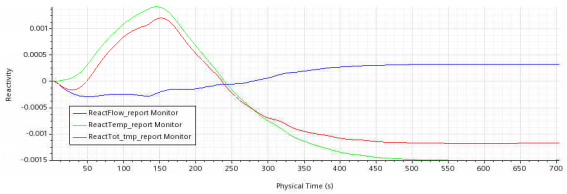

(c) Core Reactivity

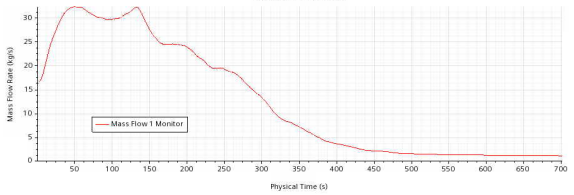

(d) Mass Flow Rate

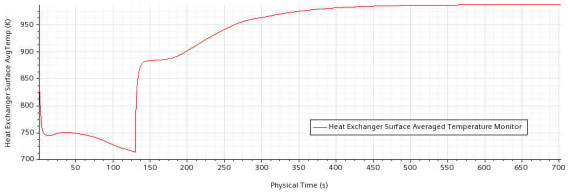

(e) Heat Exchanger Average Surface Temperature

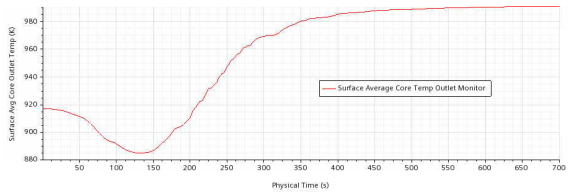

(f) Reactor Outlet Surface Averaged Temperature

Figure 5: STAR-CCM+ simulation showing overpower demand followed by loss of heat sink. Initial system power is 400 kW stead state. At time zero, the system experiences a prompt power demand increase to 4 MW for a duration of 130 seconds which corresponds to the time needed for flow reactivity dominance to subside. At time 130 seconds, the system power demand decreases to 0 kW. The initial reactor power response decreases to about 370 kW due to flow reactivity effects. At approximately 20 seconds, colder fuel salt arrives in the reactor which contributes positive reactivity. Temperature effects dominate the core power response to the remainder of the transient. The mass flow rate more than doubles in a short period of 40 seconds and decays to about 1 kg/sec after a period of approximately 10 minutes concombinate with reactor shutdown. Severe power rates do result in significant system temperature transients which contribute to high thermal stresses particularly during cooldown where stresses can be significantly limiting to thick walled the reactor vessel structures. As expected, the heat exchanger has the coldest system temperatures and severe power transient can challenge both fuel salt solubility (approximately 823 K for 18 mol% UF_4) and solidus conditions (freezing temperature of approximately 726 K) of the fuel in local regions (see fig. (e)). For this reason, active control systems must be used to mitigate the severity of such transients.

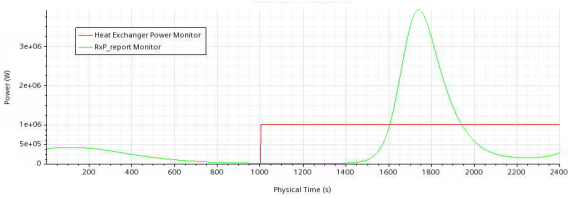

(a) Reactor and Heat Exchanger Power

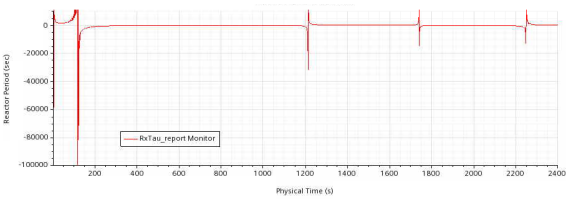

(b) Reactor Period

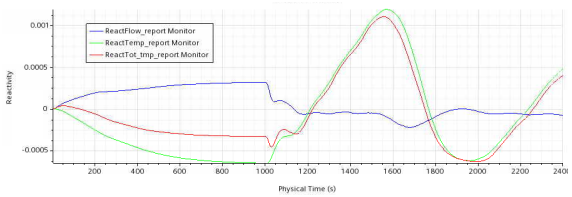

(c) Core Reactivity

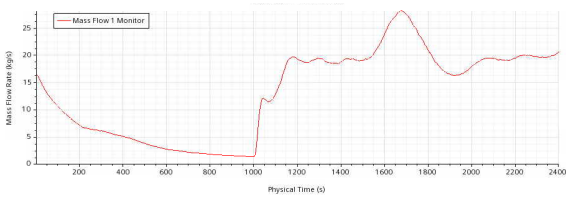

(d) Mass Flow Rate

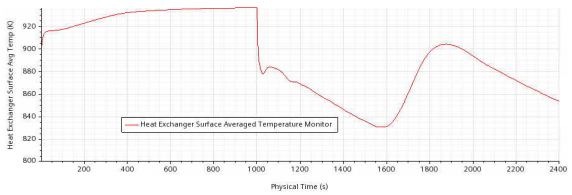

(e) Heat Exchanger Average Surface Temperature

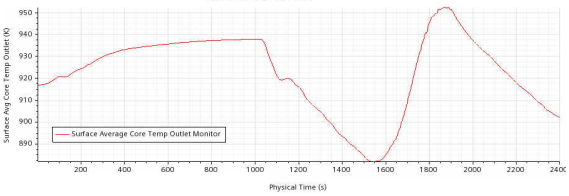

(f) Reactor Outlet Surface Averaged Temperature

Figure 6: STAR-CCM+ simulation showing effect of loss of heat sink followed by rapid restart. Initial system power is 400 kW stead state. At time zero the system experiences a prompt loss of heat sink for 1000 seconds (approximately 17 minutes). At time 1000 seconds, the system power demand increases rapidly to 1 MW. On loss of heat sink, initial core power peaks at approximately 422 kW due to flow reactivity effects. Maximum reactor outlet temperatures approach about 940 K. Upon reactor rapid startup at 1000 sec, core power reaches a minimum at approximately 1200 sec at about 388 kW before rising rapidly to a peak core power of approximately 3.8 MW. System mass flow rate response autonomously to the heat sink power demand. As in the python model, core reactivity is dominated by the temperature coefficient. Thermal transients in the heat exchanger are severe and must be evaluated in detail to ensure yield strength limitation are not approached at temperatures above the reference transition temperatures of the material involved in the design (316 SS in this case).

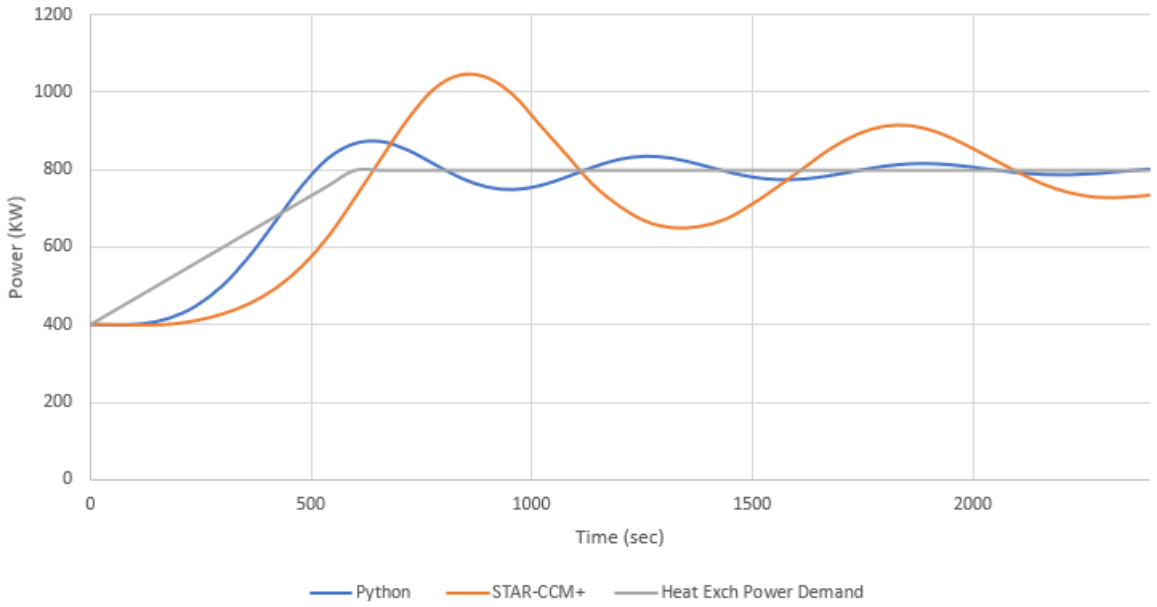

Figure 7: Comparison of simulated results for a 400 to 800 kW power demand transient response. The Python code generally provides a faster power response with reduced power overshoots and faster power damping than the CFD code in STAR-CCM+. The neutronics are the same in both codes and therefore differences can be attributed to the improved fidelity of the STAR-CCM thermal-hydraulic computations.

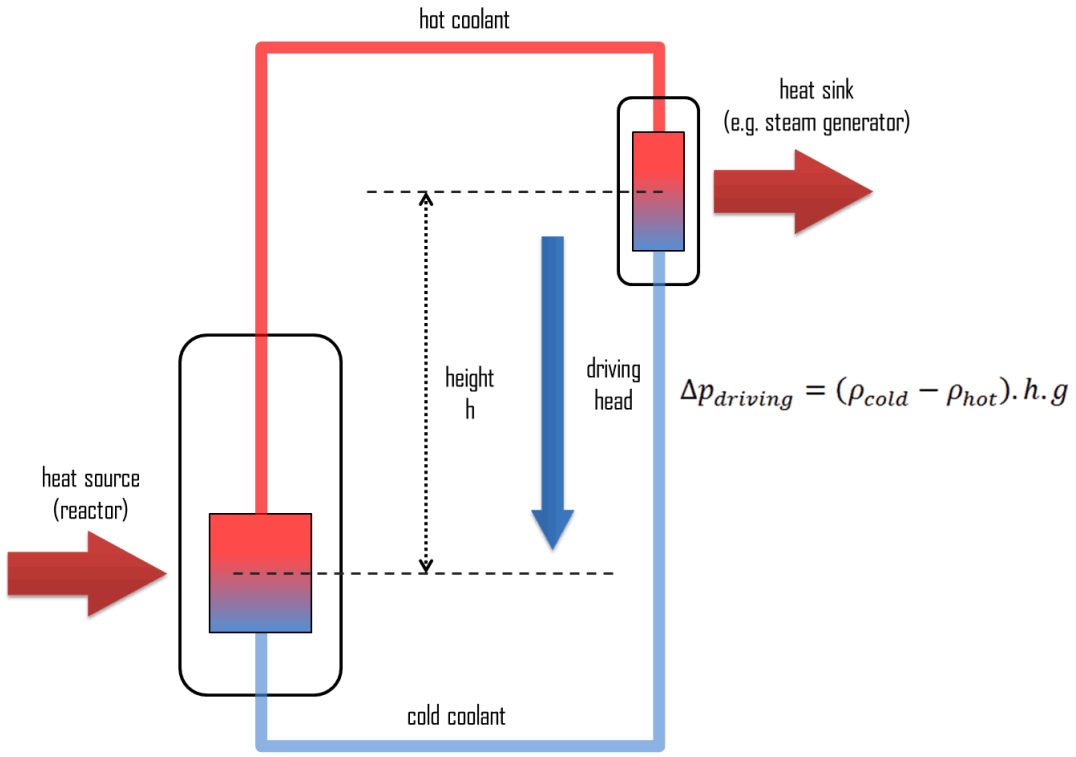

Figure 8: Simplified Natural Convection Closed Loop System. (IAEA, 2005)

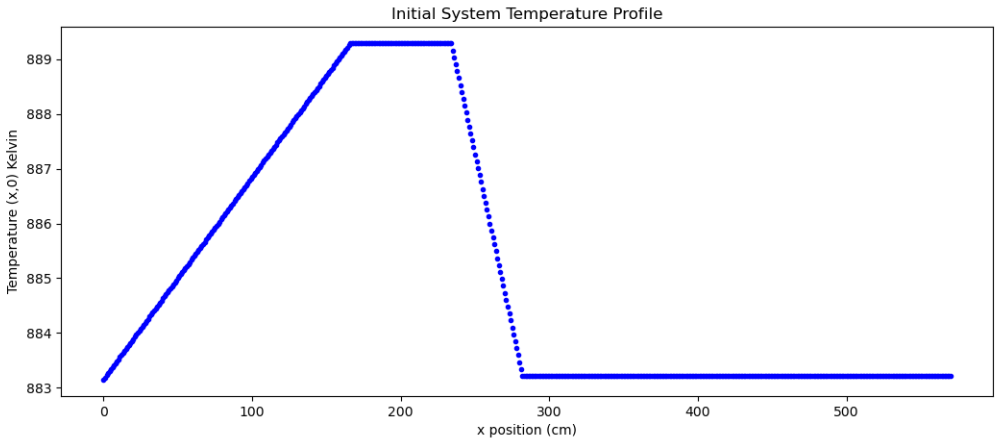

Figure 9: Initial reactor loop temperature profile. Nominal differential temperature across the reactor at 400 kWth power operation is about 5 degree Celsius. Heat generation and removal are assumed to be linear within the reactor and heat exchanger. The reactor thermodynamic control volume is assumed to be adiabatic and no preheating occurs in the downcomer flow region.

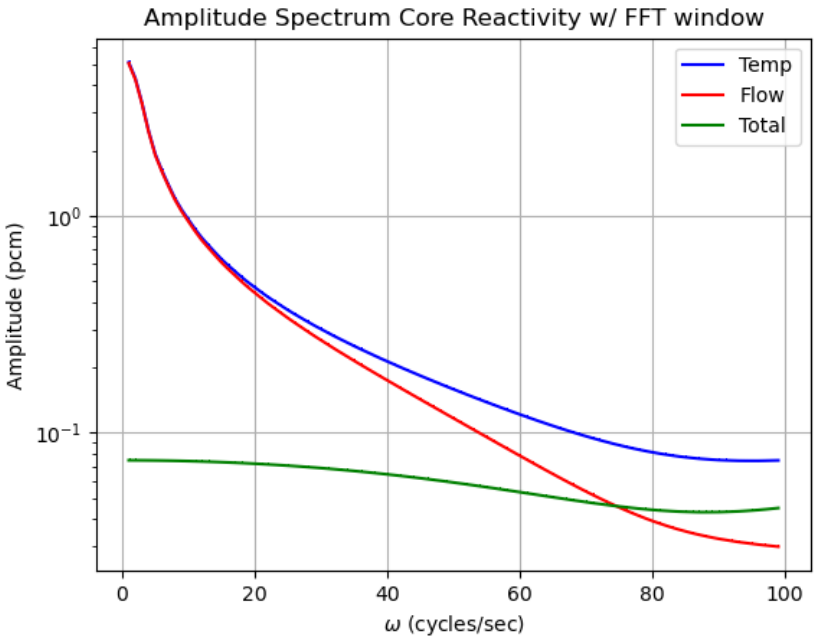

Figure 10: Stable Power Transient from 250 kW to 1000 kW over 10 minutes. Fast Fourier Transform of reactivity components. At low frequencies the temperature and flow reactivity components are out of phase. As frequency increases, the temperature component becomes the dominant contributor to overall core power behavior.

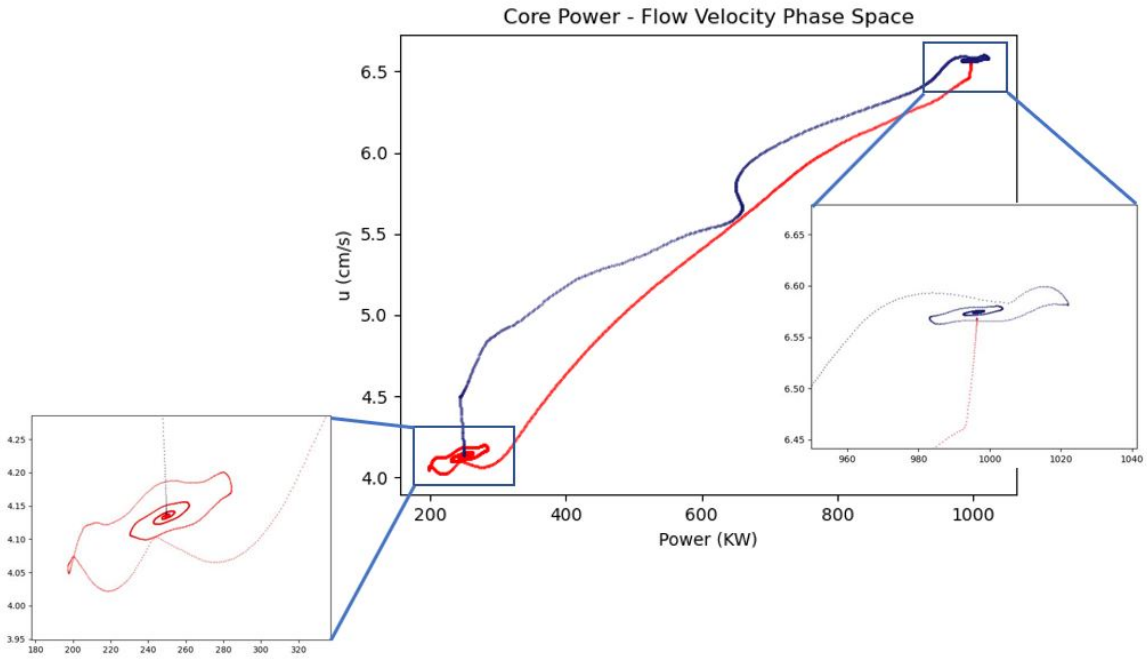

Figure 11: Power - Velocity phase space representation of a stable power transient. Up-power transient from 250 kW to 1000 kW indicated in blue. Down-power transient from 1000 kW to 250 kW indicated in red.

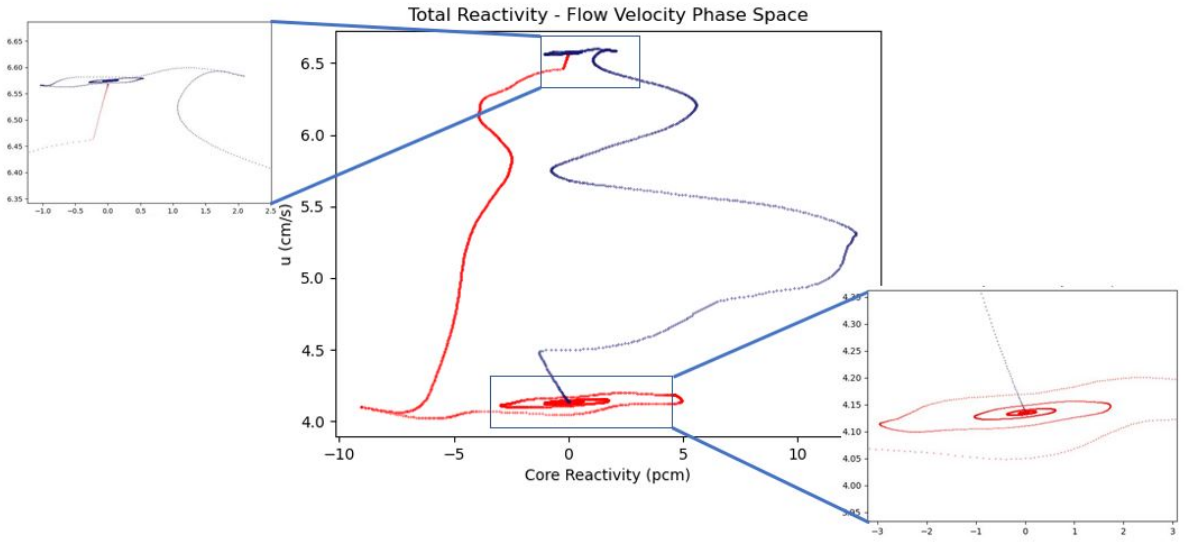

Figure 12: Reactivity - Velocity phase space representation of a stable power transient. Up-power transient from 250 kW to 1000 kW indicated in blue. Down-power transient from 1000 kW to 250 kW indicated in red.

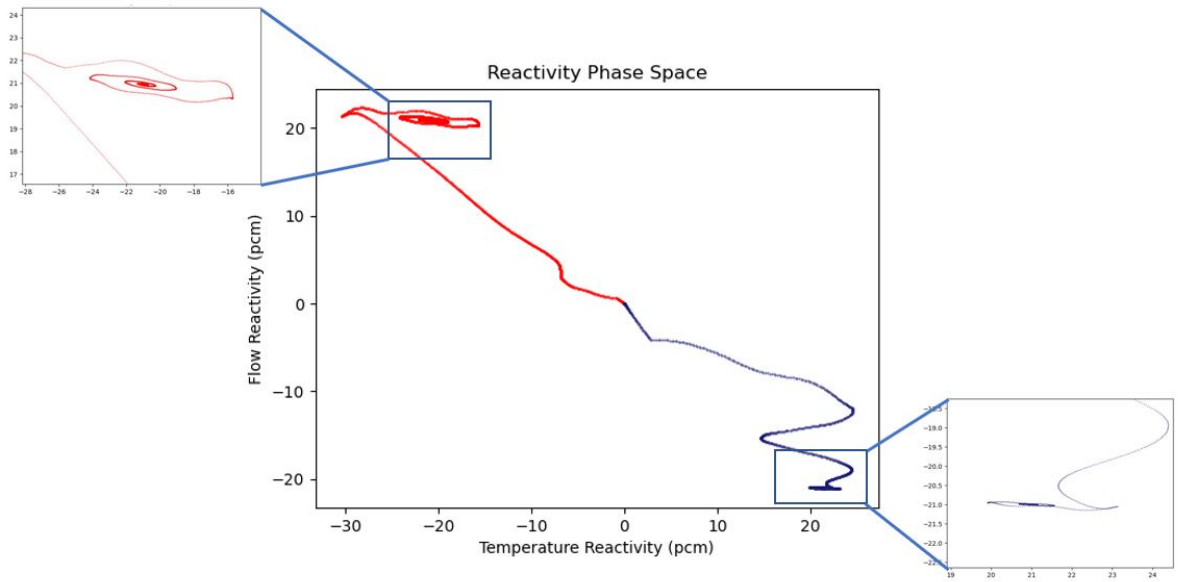

Figure 13: Temperature - Flow Reactivity phase space representation of a stable power transient. Up-power transient from 250 kW to 1000 kW indicated in blue. Down-power transient from 1000 kW to 250 kW indicated in red.

Figure 1

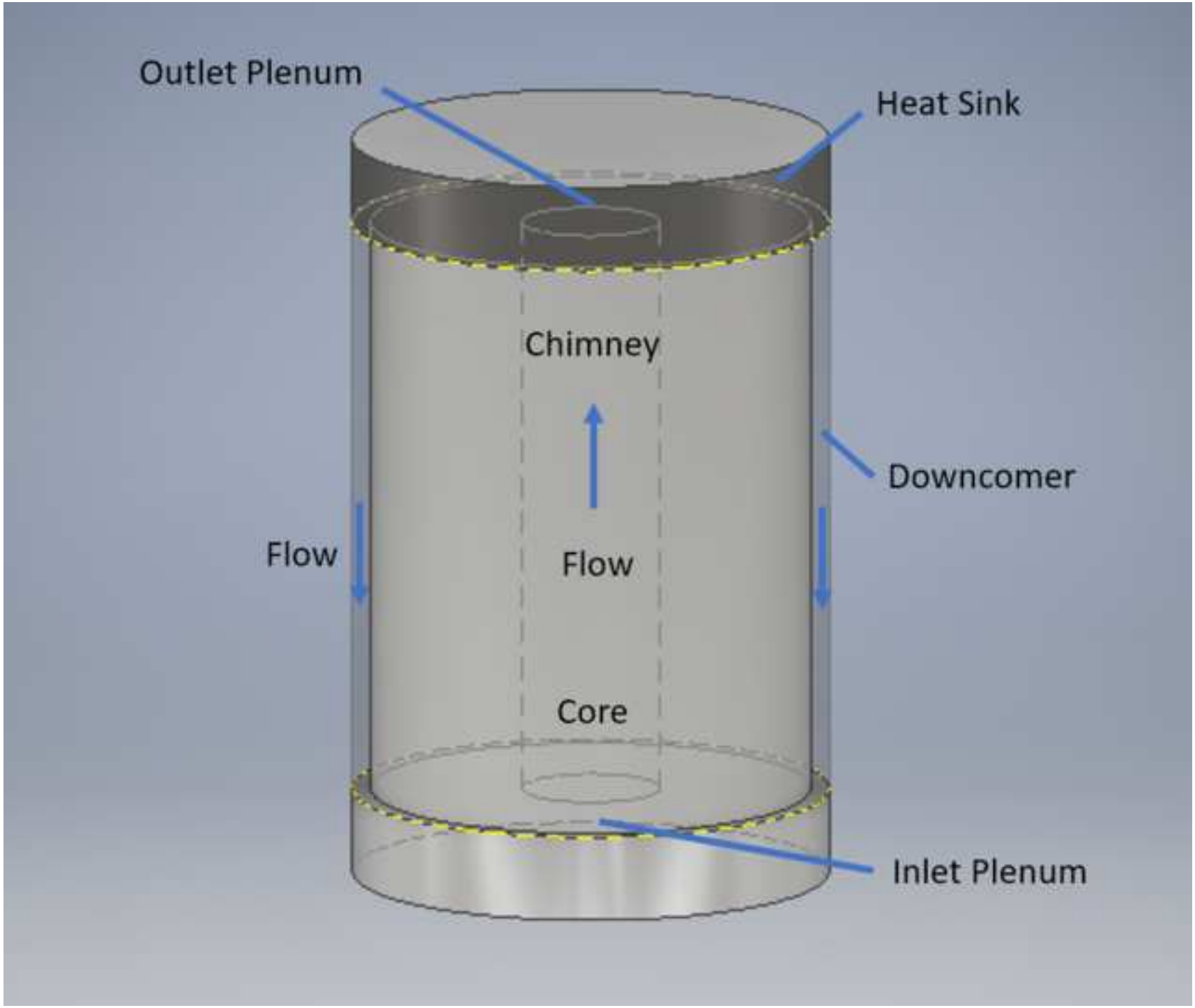

Figure 2

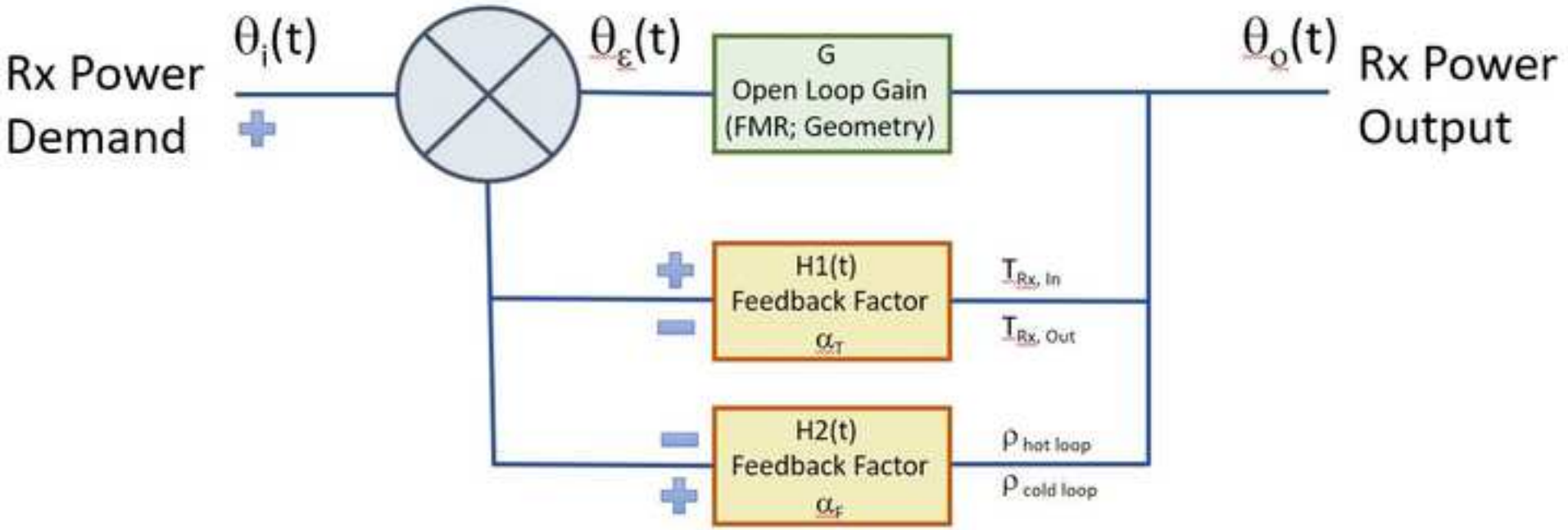

Figure 3

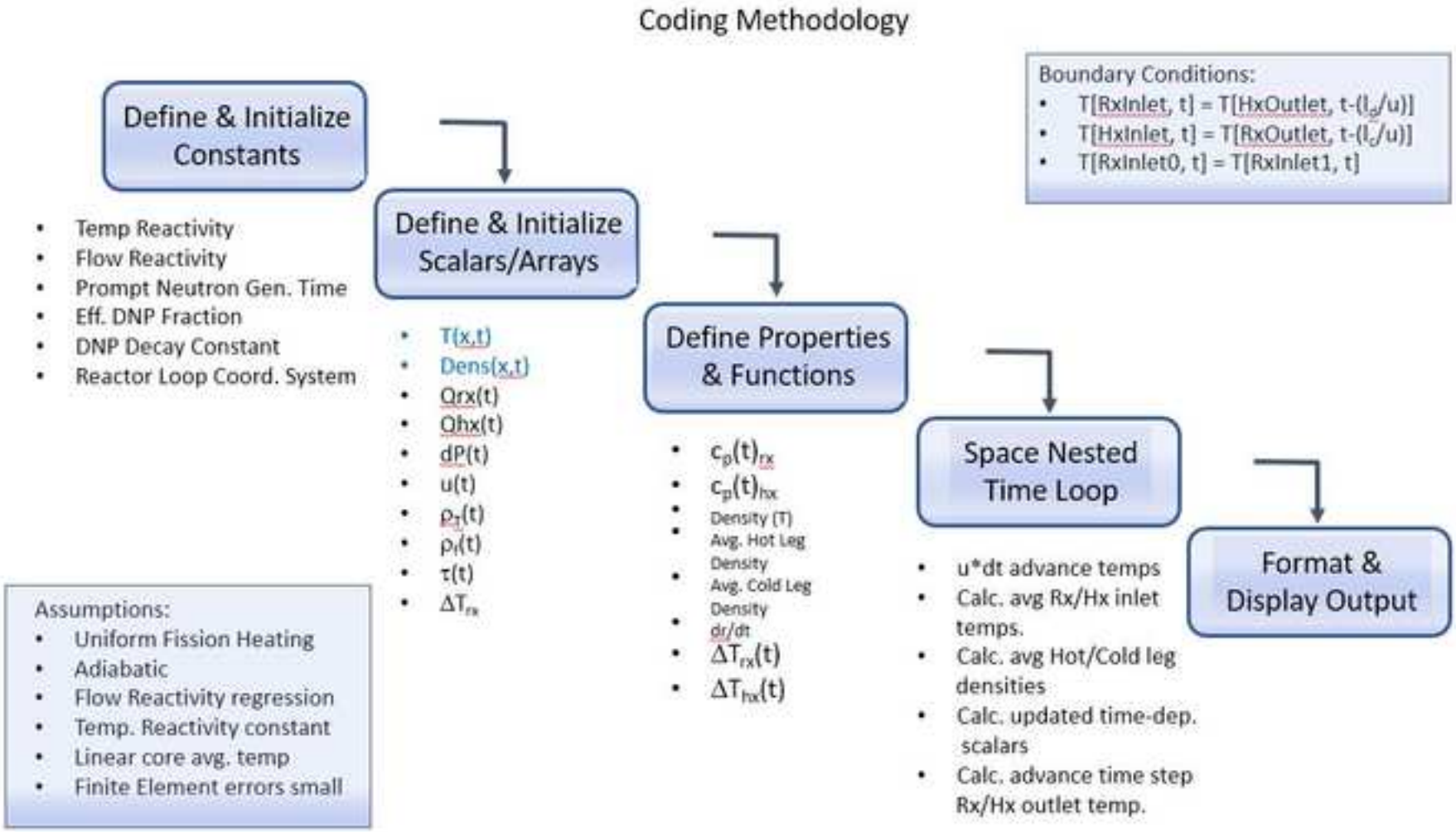

Figure 4

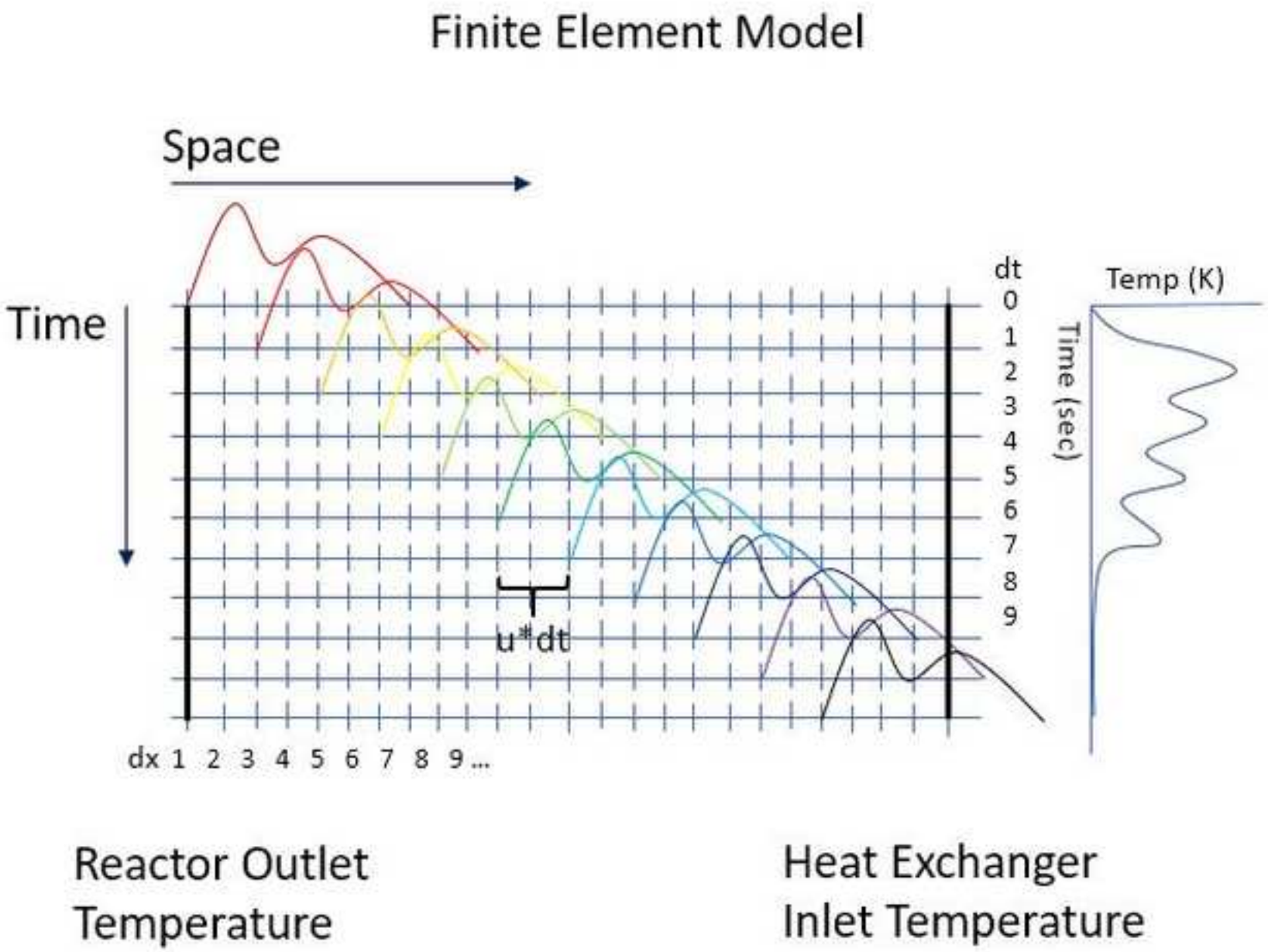

Figure 5a

Click here to access/download;Figure;Xsient_400_4000__power.PNG

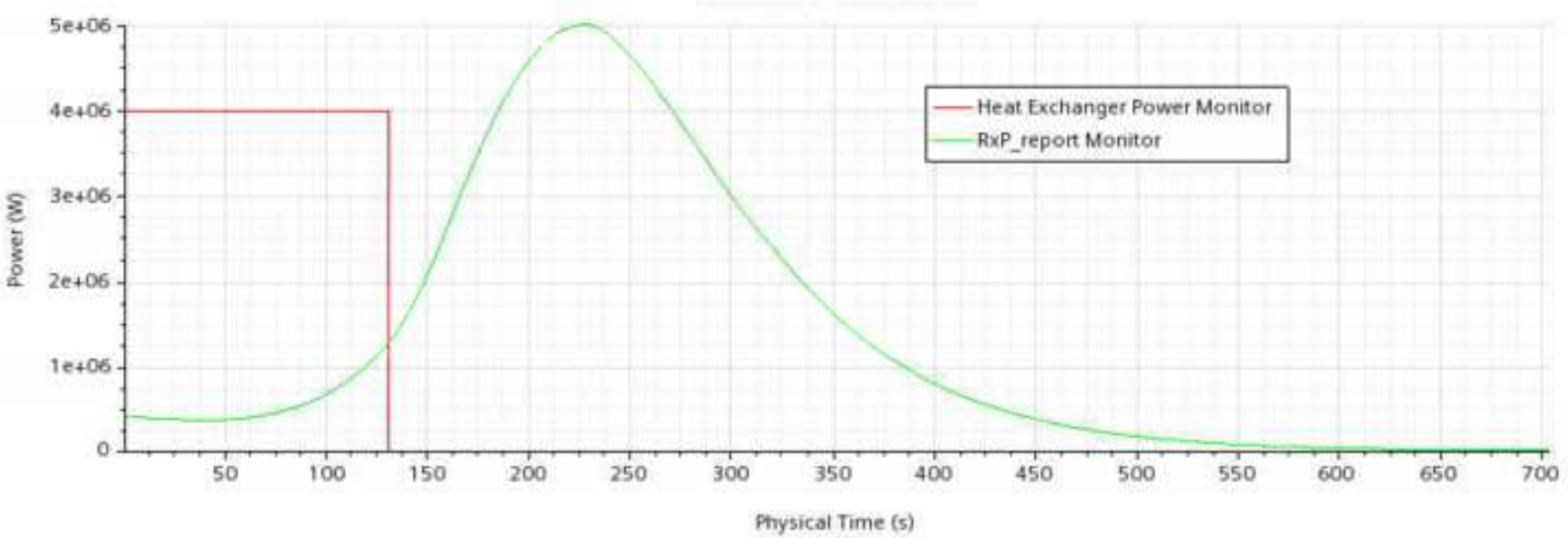

Figure 5b

Click here to access/download;Figure;Xsient_400_4000__RxPeriod.PNG

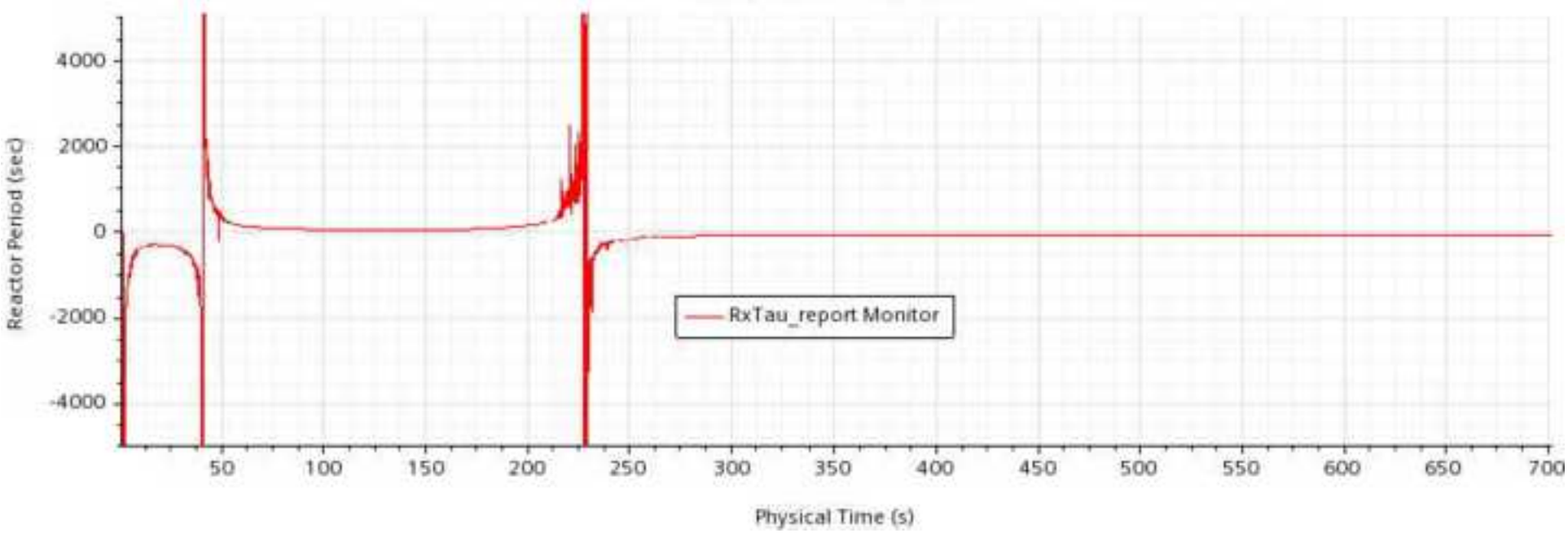

Figure 5c

Click here to access/download;Figure;Xsient_400_4000__reactivity.PNG

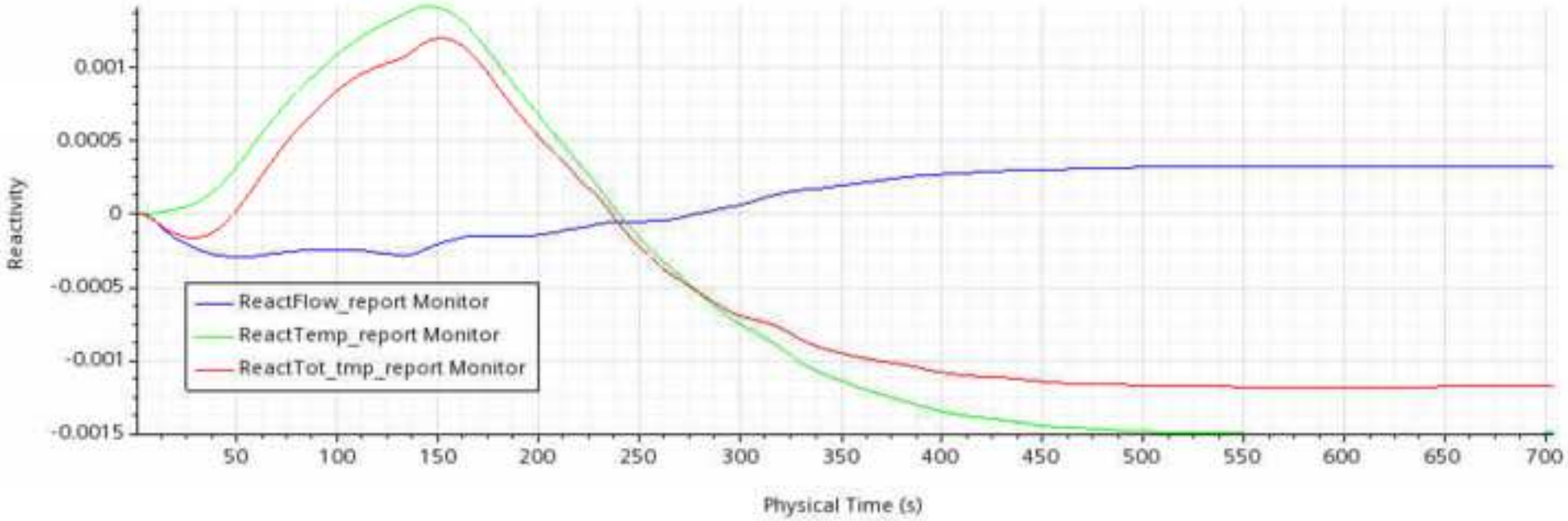

Figure 5d

Click here to access/download;Figure;Xsient_400_4000__mdot.PNG

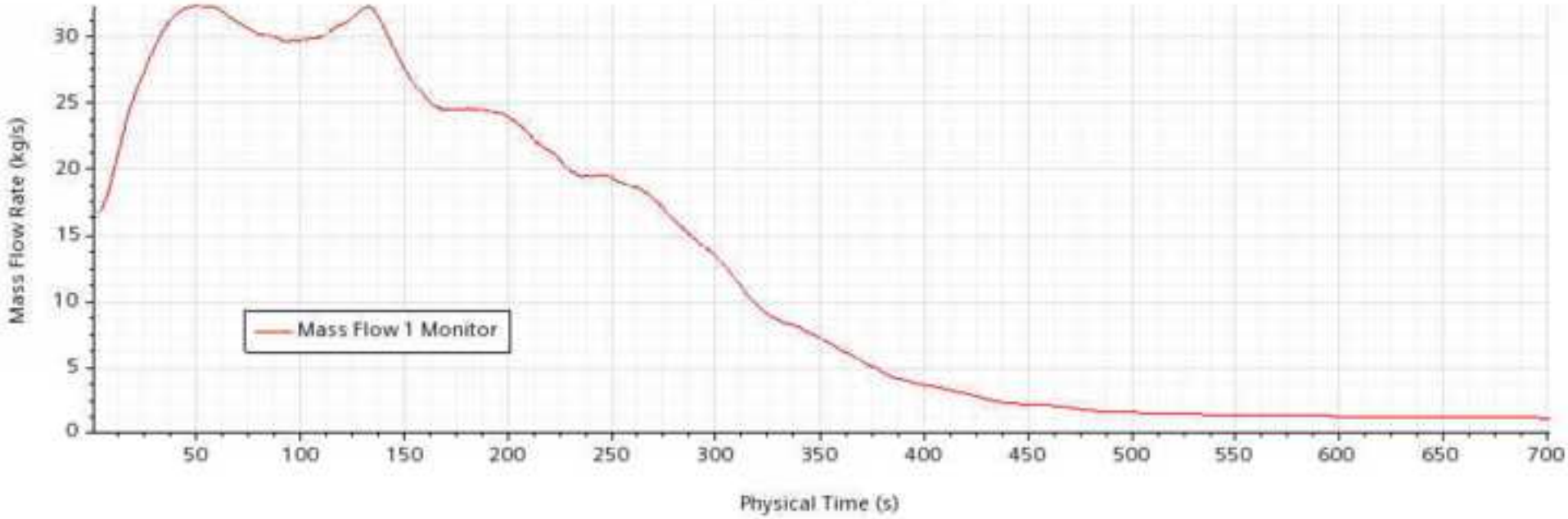

Figure 5e

Click here to access/download;Figure;Xsient_400_4000__hxsurfavgtemp.PNG

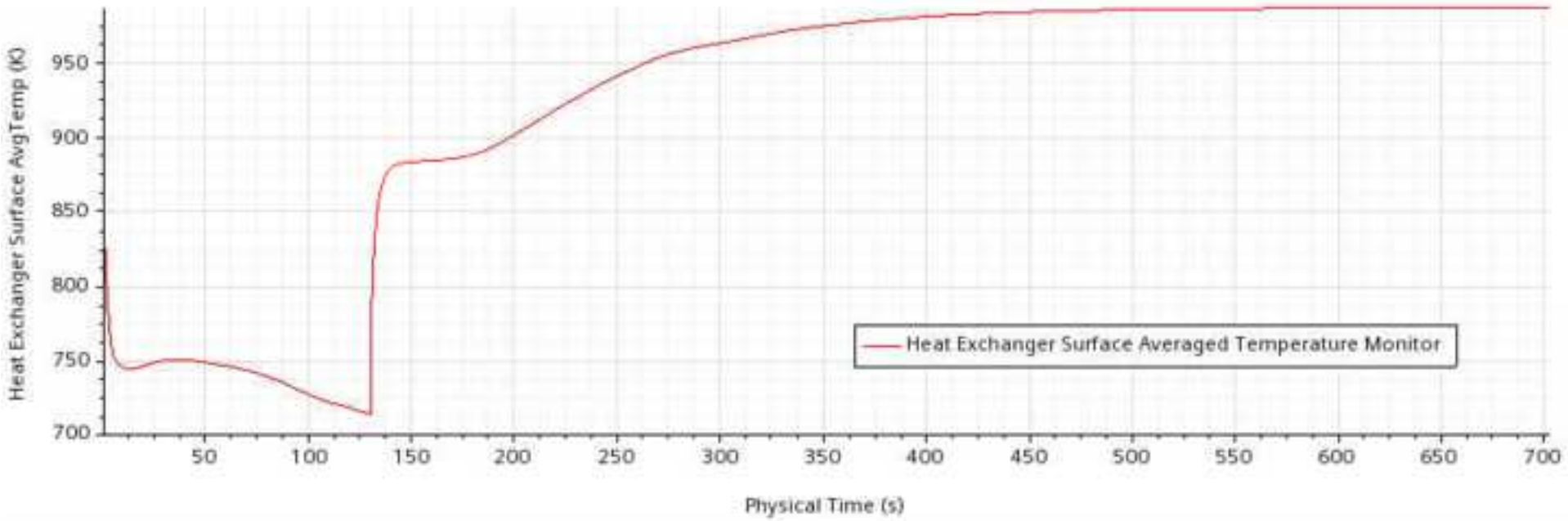

Figure 5f

Click here to access/download;Figure;Xsient_400_4000__RxAvgsurfOutletTemp.PNG

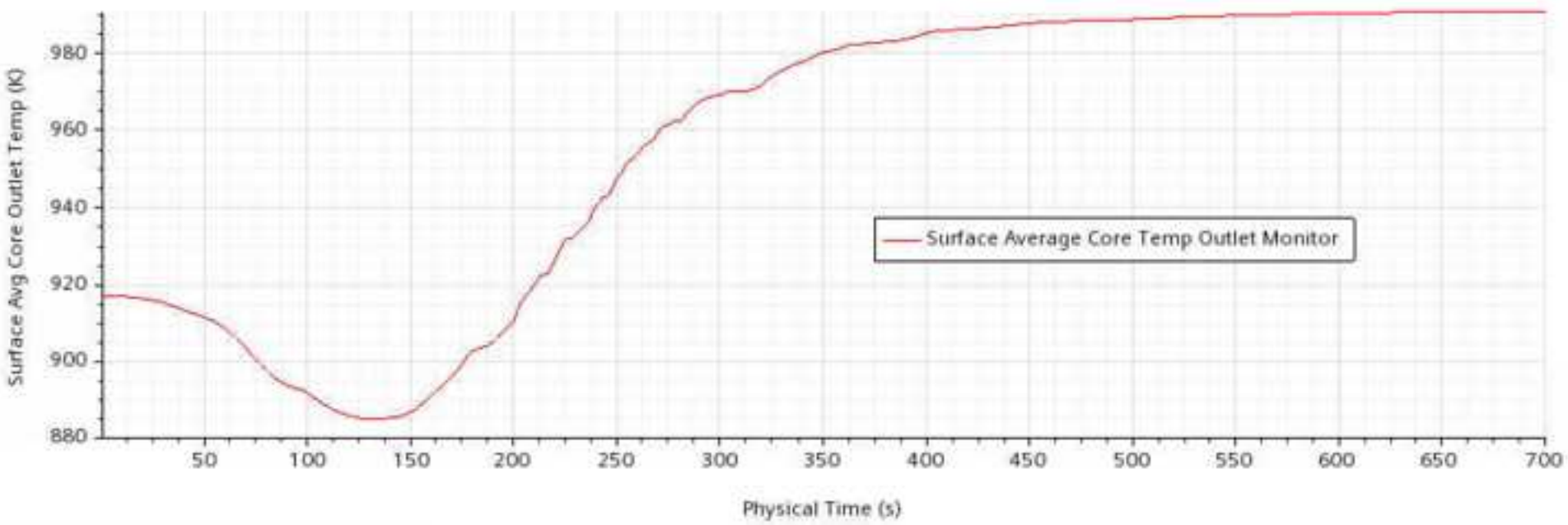

Figure 6a

Click here to access/download;Figure;Xsient_400_0_1000_pwr.PNG

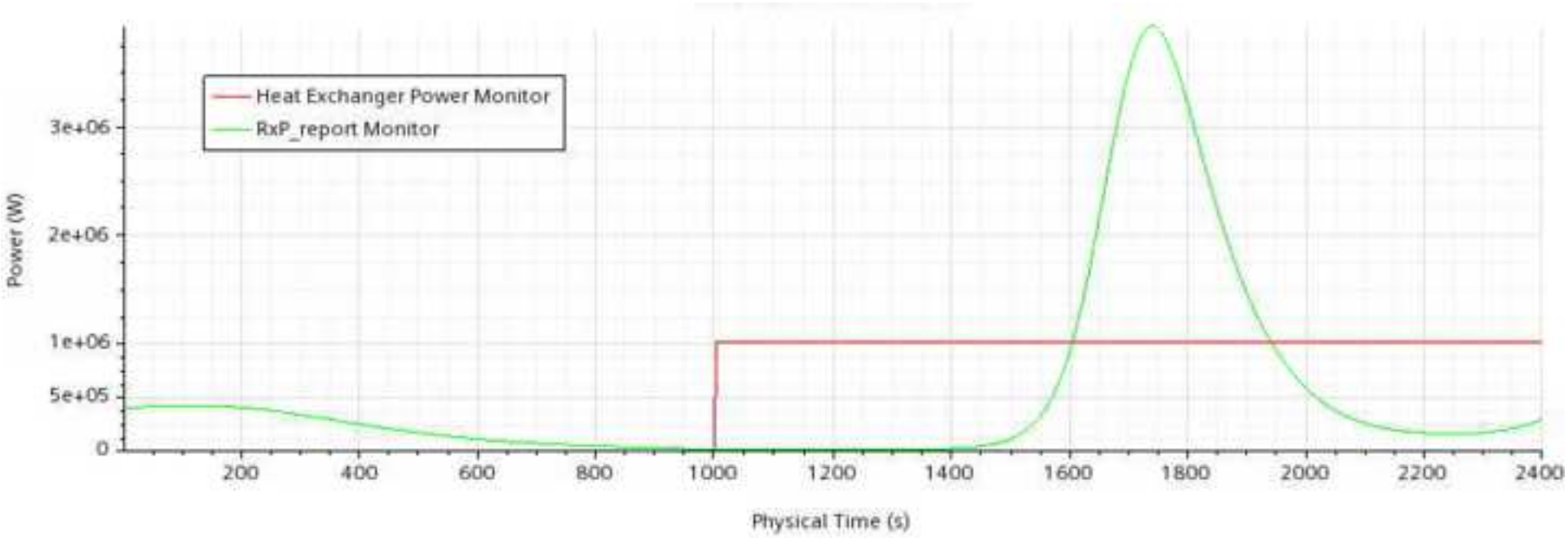

Figure 6b

Click here to access/download;Figure;Xsient_400_0_1000_RxPeriod.PNG

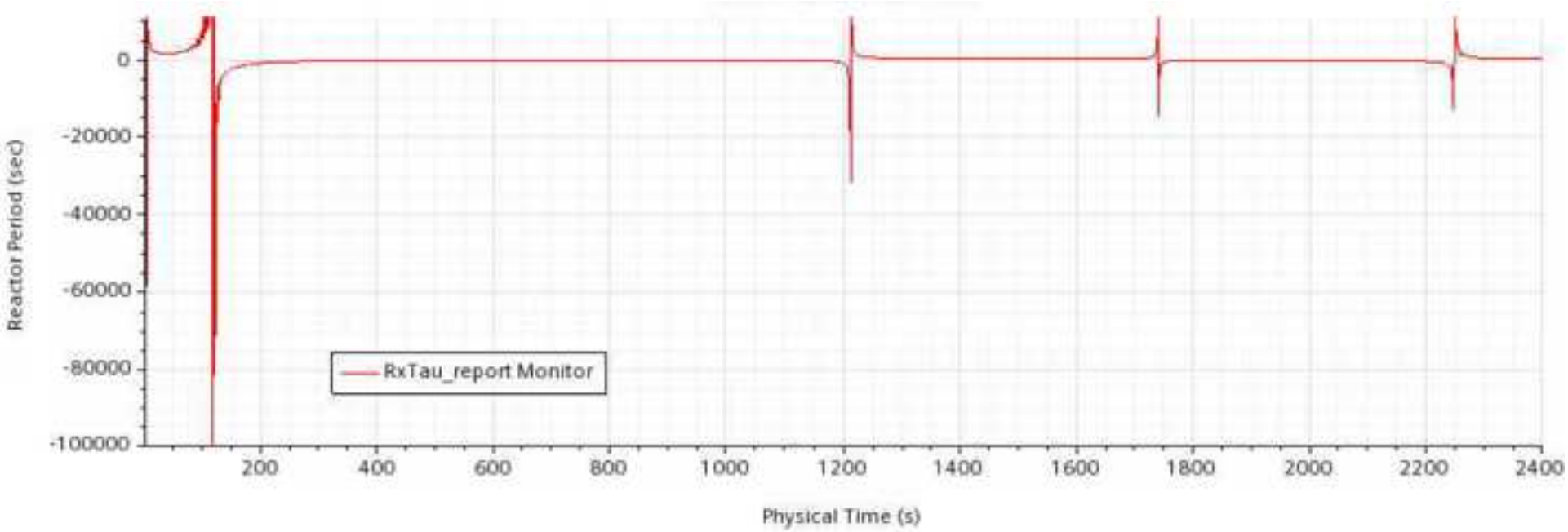

Figure 6c

Click here to access/download;Figure;Xsient_400_0_1000_rho.PNG

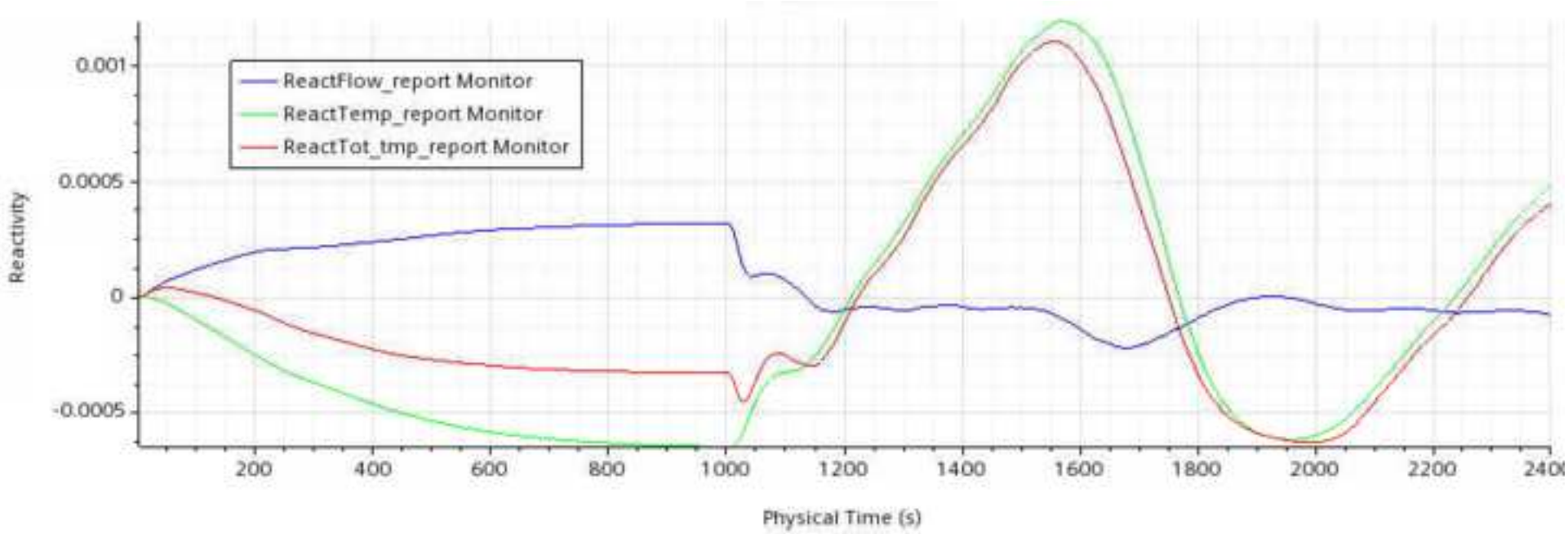

Figure 6d

Click here to access/download;Figure;Xsient_400_0_1000_mdot.PNG

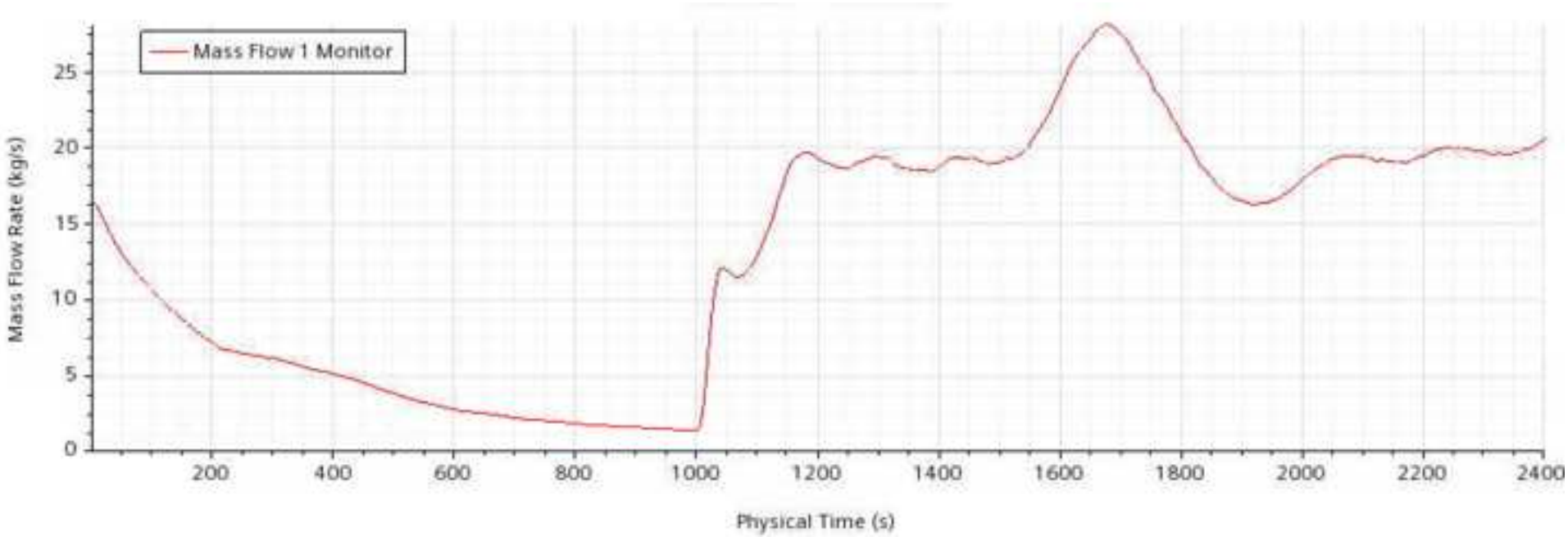

Figure 6e

Click here to access/download;Figure;Xsient_400_0_1000_hxAvgsurfTemp.PNG

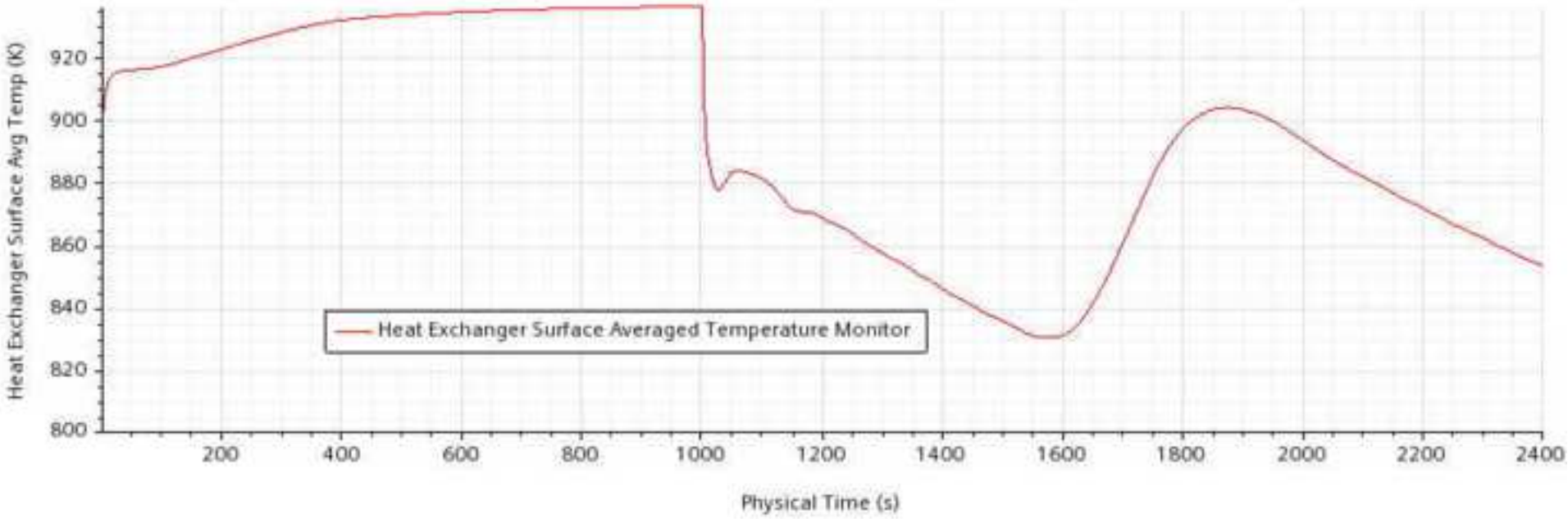

Figure 6f

Click here to access/download;Figure;Xsient_400_0_1000_RxOutletTemp.PNG

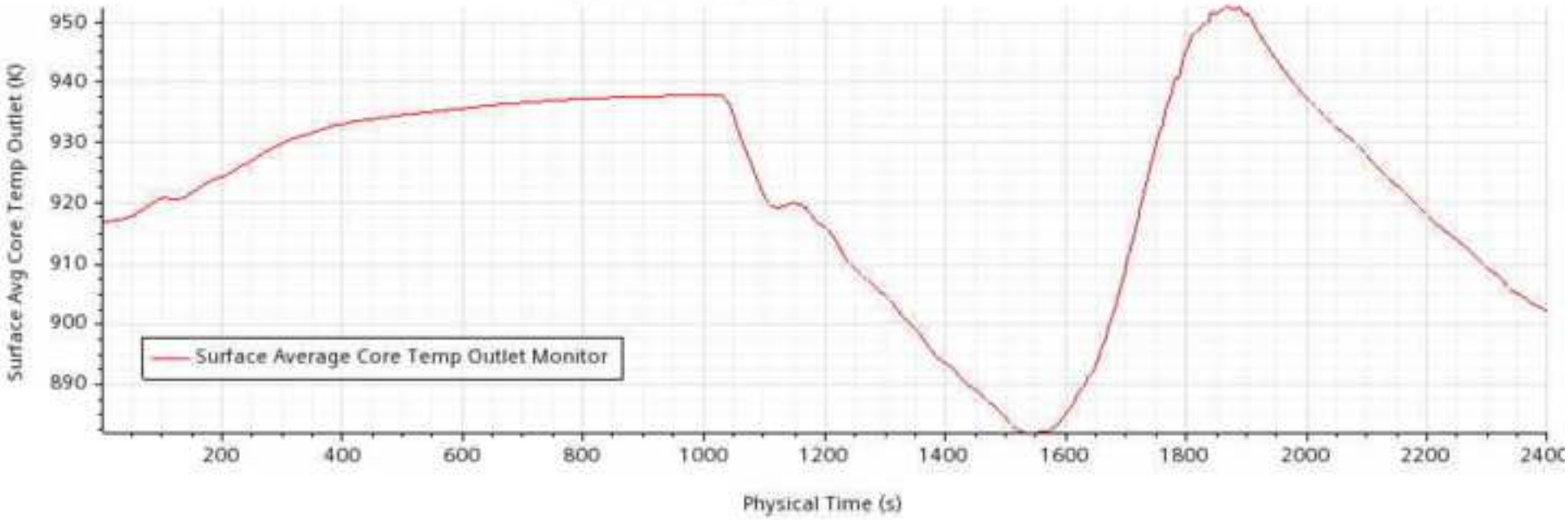

Figure 7

Click here to access/download;Figure;STAR_Python_power.PNG

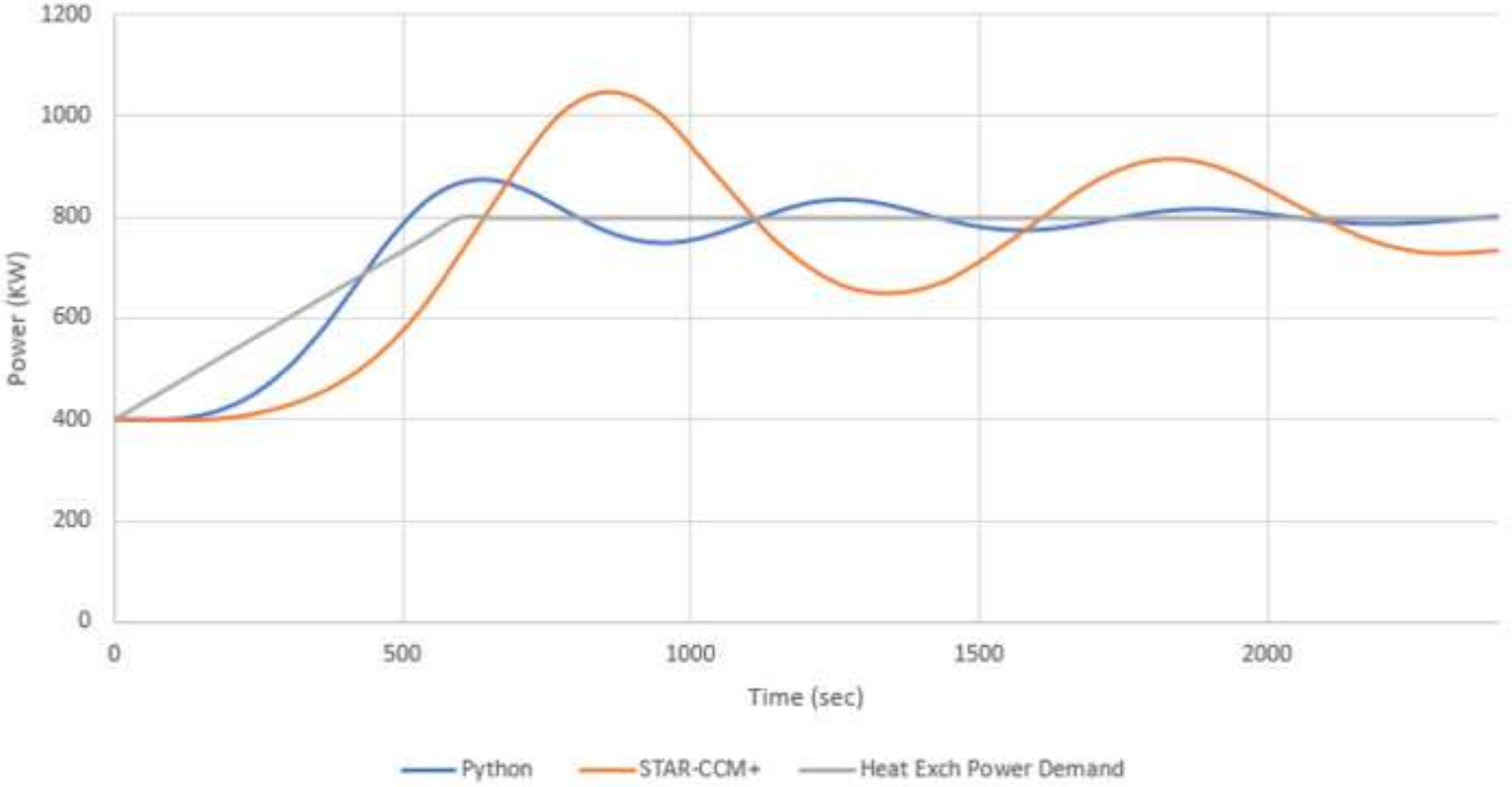

Figure 8

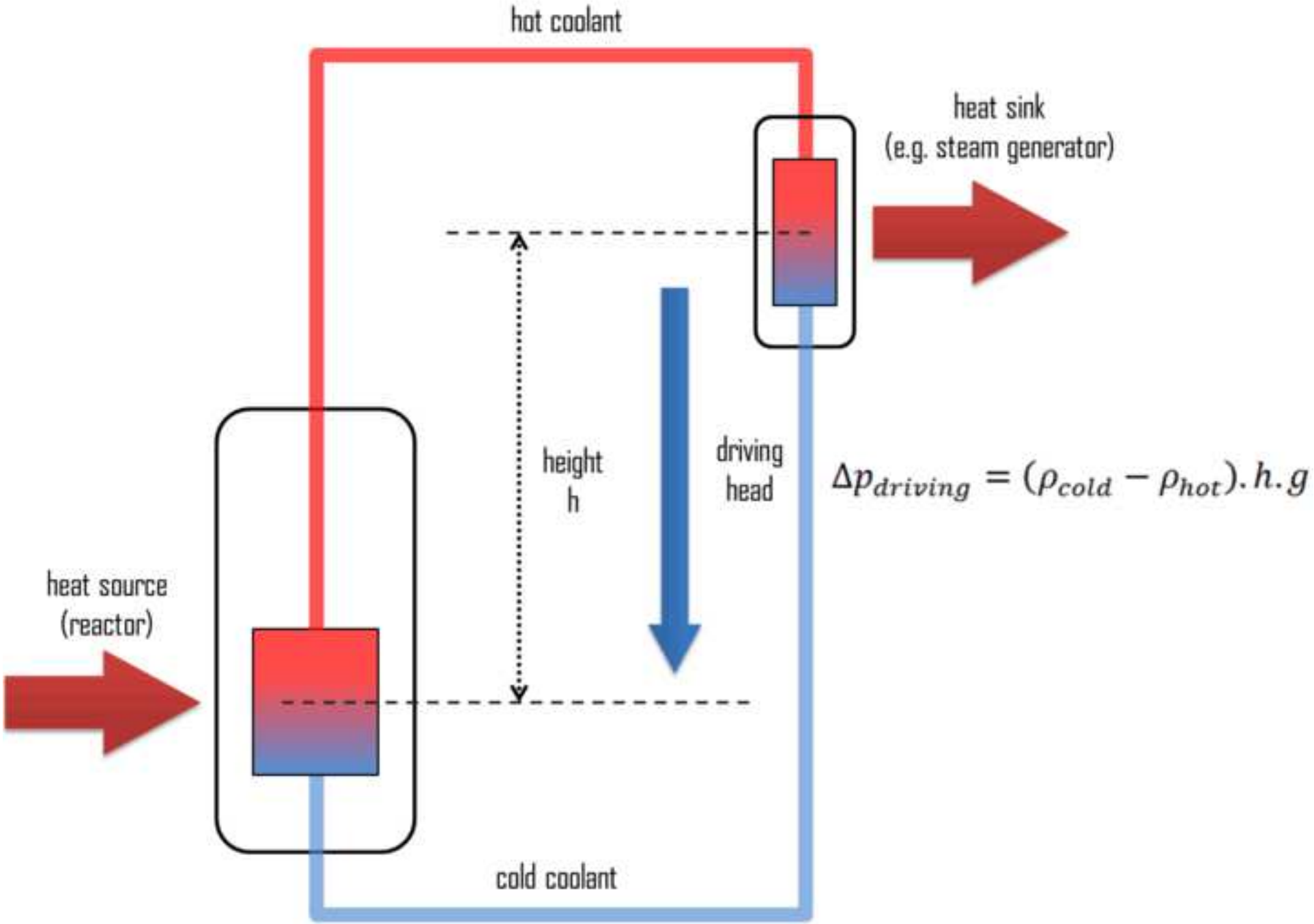

Figure 9

Click here to access/download;Figure;InitT_1.png

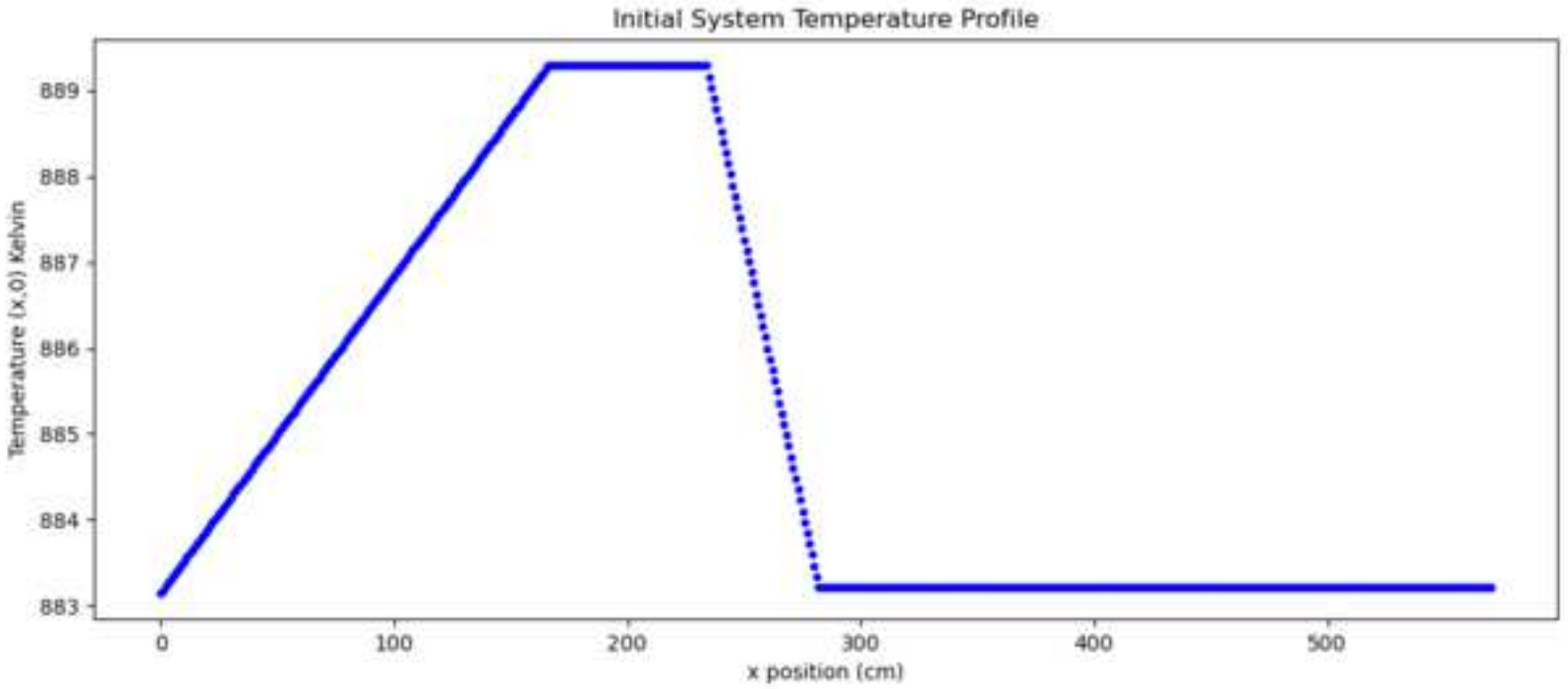

Figure 15

Click here to access/download;Figure;9a.png

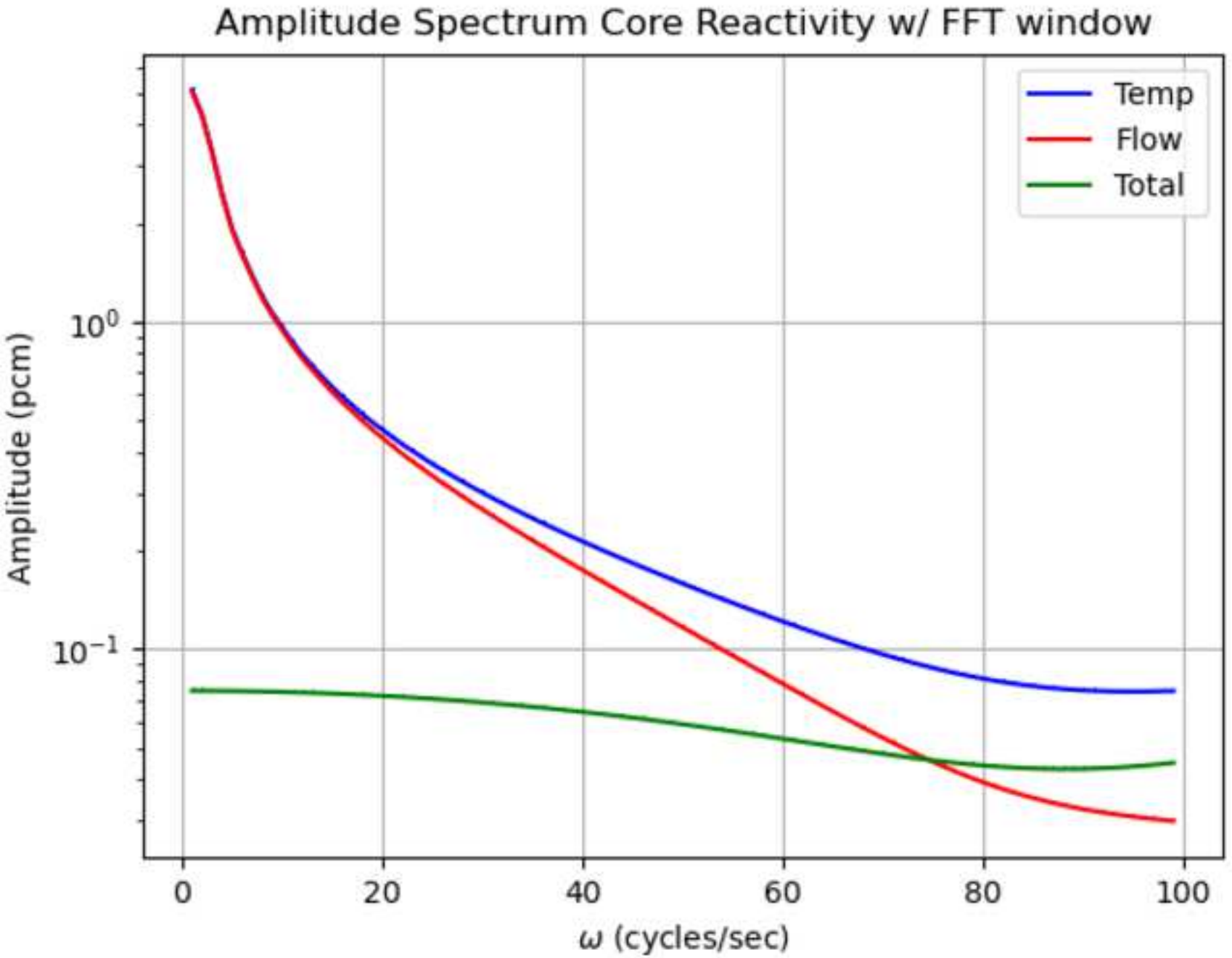

Figure 16

Click here to access/download;Figure;PiP6.JPG

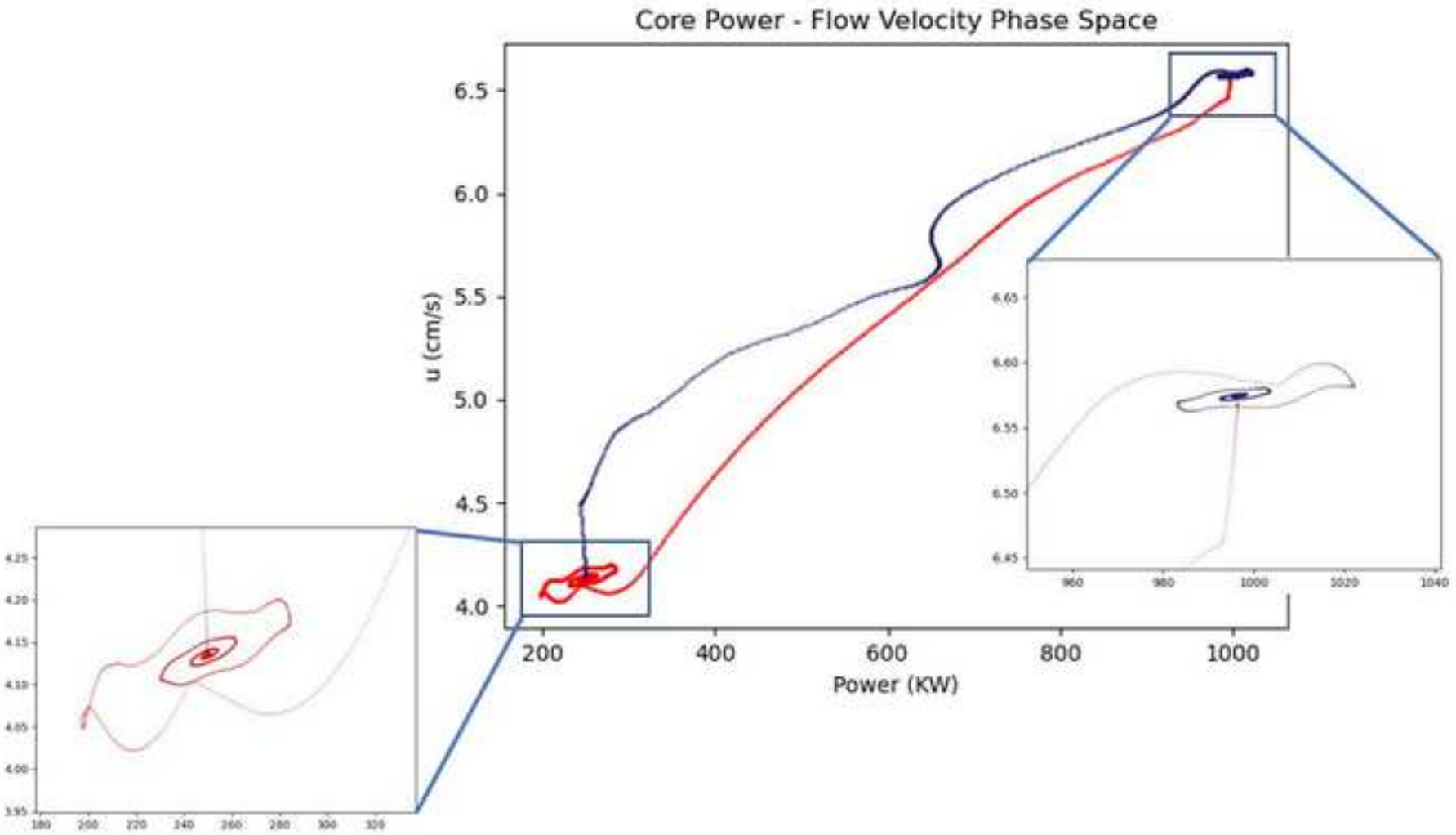

Figure 17

Click here to access/download;Figure;PiP7.JPG

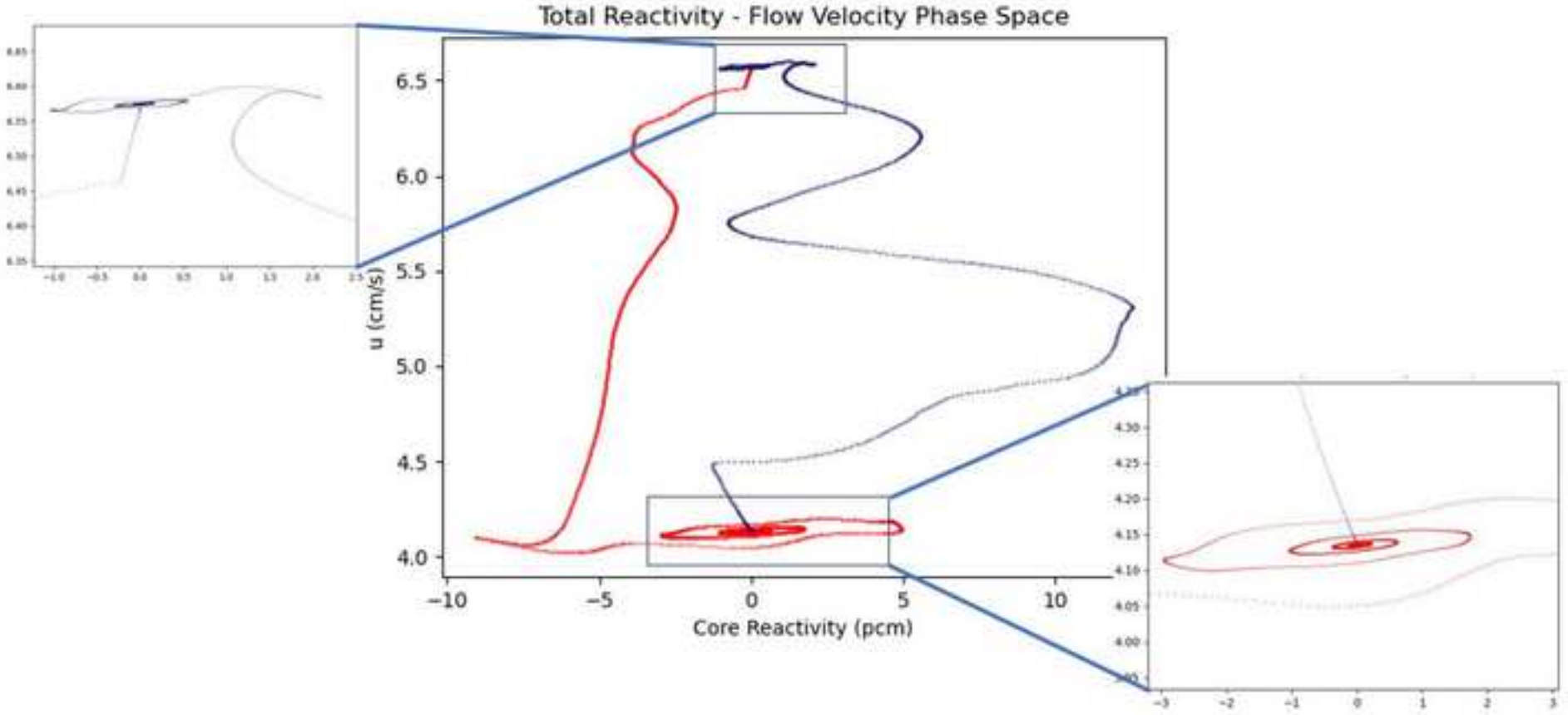

Figure 18

Click here to access/download;Figure;PiP8.JPG